FGF overactivation underlies reduced neurogenesis in cerebellar organoid models of neurodevelopmental ciliopathy

Ludovica Brunetti[1,2,*], Antonia Wiegering[1,2], Isabelle Anselme[1,2], Lidia Pollara[3,4], Martin Catala[1,2], Christophe Antoniewski[2], Enza Maria Valente[3,4], Sylvie Schneider-Maunoury[1,2,#,*], Christine Vesque[1,2,#,*]

1. Sorbonne Université, CNRS, Inserm, Development, Adaptation and Aging, Dev2A, F-75005 Paris, France
2. Sorbonne Université, CNRS, Inserm, Institut de Biologie Paris Seine, IBPS, F-75005 Paris, France
3. Department of Molecular Medicine, University of Pavia, Pavia, Italy
4. Neurogenetics Research Center, IRCCS Mondino Foundation, Pavia, Italy

# These authors jointly supervised this work

* co-corresponding authors

ABSTRACT

Cerebellar hypoplasia and dysplasia are hallmark features of neurodevelopmental ciliopathies such as Joubert syndrome. These disorders are caused by biallelic mutations in one of over 40 genes regulating the function of the primary cilium, a near-ubiquitous antenna-like organelle involved in signal reception and transduction. To date, the pathogenetic mechanisms linking ciliary gene dysfunction to Joubert syndrome neurodevelopmental defects are poorly understood. In this study, we generate cerebellar organoids from human induced pluripotent stem cells carrying either null mutations or patient-derived variants in *RPGRIP1L*, a Joubert syndrome causal gene encoding a scaffold protein crucial for ciliary function. While control organoids robustly express markers of cerebellar glutamatergic and GABAergic lineages including Purkinje cells, *RPGRIP1L*-deficient organoids display a consistent and severe reduction in Purkinje cell markers, along with impaired neurogenesis and increased progenitor proliferation. These defects coincide with prolonged overactivation of the FGF signaling pathway. Pharmacological inhibition of FGF signaling rescues both the proliferative/neurogenic balance and Purkinje lineage formation in *RPGRIP1L*-deficient organoids. Thus, our findings uncover early FGF pathway deregulation as a key driver of cerebellar differentiation defects in an *in vitro* model of Joubert syndrome, providing new insight into the developmental origin of cerebellar impairment in neurodevelopmental ciliopathies.

INTRODUCTION

Cerebellar dysfunction is a common feature of several developmental disorders, associated with both motor disease and cognitive impairment [1]. The cerebellum originates from dorsal hindbrain rhombomere 1 (r1) under inductive cues from the isthmic organizer at the midbrain–hindbrain boundary, where fibroblast growth factor 8 (FGF8) expression defines the early cerebellar territory [2–4]. Two distinct germinal zones subsequently form: the ventricular zone (VZ), which produces inhibitory GABAergic neurons such as Purkinje, Golgi, and basket cells [5], and the rhombic lip (RL), which generates excitatory glutamatergic lineages including granule neurons (GNs) and unipolar brush cells [6,7]. In humans, Purkinje cell neurogenesis occurs between post-conception weeks (PCW) 8–10 [8,9], whereas granule cell progenitors (GCPs) proliferate extensively around 26 PCW [10]. Coordinated proliferation and differentiation of these populations are critical for establishing cerebellar size, morphology, and function [11].

Joubert syndrome (JBTS) is a rare neurodevelopmental disease affecting the cerebellum and brainstem, primarily characterized by hypoplasia/dysplasia of the vermis – the medial cerebellar structure. All JBTS patients share the diagnostic “molar tooth sign” on axial brain imaging, resulting from specific cerebellar and brainstem malformations [12,13]. Clinically, patients present with ataxia, ocular motor defects, developmental delay, and intellectual disability [14]. Over 40 causative genes have been identified, all encoding proteins involved in primary cilia structure or function [13,15]. Primary cilia are microtubular sensory organelles protruding from the surface of almost all vertebrate cells, acting as signaling hubs [16–18]. To ensure proper signaling their composition is controlled by the transition zone, composed of protein complexes such as the MKS, NPHP (NPHP1, NPHP4, NPHP8/RPGRIP1L), and CEP290 modules [19,20]. Among them, the JBTS gene *RPGRIP1L* encodes a scaffolding protein essential for transition zone integrity [21,22] and HH pathway activity [23,24]. Mutations in *RPGRIP1L* can also cause the more severe Meckel syndrome.

In the cerebellum, ciliogenesis is temporally regulated to ensure appropriate responsiveness to SHH and other signals [25–27]. In mice, a loss of cilia in the brain causes cerebellar hypoplasia and foliation defects due to loss of SHH-dependent GCP proliferation [28,29], while mouse

96 mutants for JBTS genes — including *Rpgrip1l* [30], *Ahi1* [31], *Tmem67* [32], *Jbts17 (CPLANE1)* [33],
97 *Talpid3* [34], *Arl13b* [35] and Cep290 [31] — exhibit variable cerebellar phenotypes and divergent
98 effects on HH and WNT signaling. In humans, the analysis of JBTS fetal samples with a
99 confirmed diagnosis of cerebellar vermis hypoplasia revealed a reduction of GCP proliferation
100 associated with a lower expression of HH targets, with no differences between hemispheres
101 and vermis. These findings suggest that the specific vermis hypoplasia observed in JBTS
102 patients precedes and is independent of GCP proliferation defects, leaving its primary origin
103 unresolved [36]. Overall, the pathogenetic mechanisms linking cilia dysfunction to JBTS
104 neurodevelopmental defects remain largely unknown and may be of diverse origins.
105
106 This leaves us with several open questions: i) what are the early cellular and molecular
107 processes affected by JBTS gene depletion during human cerebellar development? ii) can
108 some of these defects account for cerebellar vermis hypo/dysplasia observed in JBTS patients?
109 iii) can we identify drug treatments that could potentially alleviate JBTS disease
110 manifestations? In order to address these questions, we turned to human iPSC-derived
111 cerebellar organoids, recently established as promising approaches to study human cerebellar
112 development and neurodevelopmental diseases [37–44]. By recapitulating developmental
113 pathways, these approaches are particularly well suited to study early steps of cerebellar
114 development. Moreover, in a previous work we demonstrated significant differences
115 concerning cilia formation and function in human and mouse spinal organoids in the absence
116 of JBTS proteins (RPGRIP1L and TMEM67) [45], further emphasizing the importance of using
117 human-based systems to investigate the developmental origin of cilia-related cerebellar
118 defects.
119
120 Here, we employ human iPSC-derived cerebellar organoids to investigate the role of *RPGRIP1L*
121 in cerebellar development. We chose *RPGRIP1L* for its central role in ciliary transition zone
122 assembly and severe brain defects in mouse models [46]. Using organoids derived from JBTS
123 patient iPSCs carrying biallelic *RPGRIP1L* mutations and CRISPR-engineered knockouts, we
124 uncover early ciliary abnormalities, morphological alterations, and aberrant FGF signaling
125 activation. Excessive FGF activity drives progenitor hyperproliferation and impaired
126 neurogenesis, defects that are rescued by pharmacological FGF inhibition after midbrain-
127 hindbrain boundary induction.

128 Our findings reveal a causal link between *RPGRIP1L* dysfunction, dysregulated FGF signaling,
129 and disrupted cerebellar neurogenesis, providing mechanistic insight into the developmental
130 origin of cerebellar malformations in JBTS.

131 **RESULTS**

132

133 ***Cerebellar organoids generated from human induced pluripotent stem cells recapitulate***
134 ***early steps of cerebellar development***

135 To unravel molecular mechanisms and biological processes that may be responsible for
136 cerebellar defects in JBTS pathogenesis, we used organoids to model early stages of human
137 cerebellar development *in vitro*. We optimized published protocols for generating cerebellar
138 organoids from human induced pluripotent stem cells (hiPSCs) [37,39]. To induce neural
139 commitment, mid-hindbrain boundary establishment and tissue self-organization, embryoid
140 bodies were sequentially treated with fibroblast growth factor 2 (FGF2), insulin, TGFß/SMAD
141 inhibitor (SB431542), FGF19 and stromal cell-derived factor 1 (SDF1) (**Fig. 1A).** Since dynamic
142 culture conditions have been shown to favor faster cerebellar commitment [47], embryoid
143 bodies were cultured under orbital agitation from day 7 onwards.

144 Immunostaining analysis on control organoid cryosections showed clusters of neural
145 progenitors ($SOX2^+$) and early-born neurons (HUC/D^+), already present at day 14
146 (**Supplementary Fig. 1A**), progressively expanding and self-organizing (**Supplementary Fig.**
147 **1A-C**). By day 28, early-born neurons are primarily located in deep regions of the organoid
148 tissue, adjacent to an outer layer of neural progenitors organized either at the organoid
149 periphery or into small internal rosettes (**Supplementary Fig. 1C**).

150 To assess the time-course of cerebellar cell type production in our experimental settings, we
151 performed bulk RNAseq analysis on cerebellar organoids derived from two independent
152 control hiPSC lines with different genetic backgrounds, PCIi033-A (Ph2) and UCSFi001-A
153 (Wtc11) at the hiPSC stage (day 0) and at five timepoints of the differentiation protocol (day
154 7, 14, 21, 28, 35) (see **Supplementary Excel File 1** for normalized gene expression data). First,
155 we validated that the control organoids faithfully recapitulated early stages of cerebellar
156 development, with the presence of midbrain, hindbrain and mid-hindbrain boundary markers
157 and the absence of anterior forebrain and posterior hindbrain markers **(Figure 1C)**. Concerning
158 cerebellar differentiation, the order of appearance of GABAergic Purkinje lineage markers
159 reflected the *in vivo* maturation stages of this cell population, with the progenitor marker
160 *OLIG2* and the early post-mitotic marker *SKOR2* peaking at day 21, followed by the more
161 mature Purkinje marker *CALB1*, strongly expressed between day 28 and 35 **(Supplementary**
162 **Fig 1D)**. As for the glutamatergic lineage, the RNA levels of progenitor markers were gradually

163 increased over time, first appearing at day 7 for *PAX6* and *BARHL1*, and at day 14 for *ATOH1*
164 **(Supplementary Fig. 1E**). Of note, the mature GN marker, *GABRA6*, was not detected over the
165 35 days short-term organoid culture, consistent with its post-natal onset in humans [9,48]
166 **(Supplementary Fig. 1F)**. Given the well-established role of the SHH pathway in GCP pool
167 expansion during cerebellar development [49,29], we also examined SHH ligand expression.
168 However, almost no *SHH* mRNA was detected over the 35 days of cerebellar differentiation
169 **(Supplementary Fig. 1G)**. Immunostaining analysis showed that the GCP marker BARHL1 and
170 the Purkinje marker CALB1 segregated in separated domains within the organoid tissue, with
171 few cells intermingled **(Supplementary Fig. 1H)**.
172 Altogether these data provide strong evidence for self-organization of a cerebellar
173 primordium and successful specification of the two main cerebellar lineages following our
174 differentiation protocol. They also show that this 35-days differentiation protocol models early
175 cerebellar developmental stages, preceding SHH endogenous expression by Purkinje cells.
176
177 ***RPGRIP1L KO and JBTS patient-derived cerebellar organoids present a severe reduction of***
178 ***Purkinje Cell markers and a milder decrease in Granule Cell Progenitor markers***
179 To compare the differentiation process between healthy and JBTS pathological conditions, we
180 used two independent *RPGRIP1L* KO hiPSC lines – generated in the two different genetic
181 backgrounds previously used for control organoid analysis (Ph2 and Wtc11) [45] – both
182 producing early truncated proteins within the first coiled coil domain **(Fig. 1B)**. In parallel we
183 also analyzed a hiPSC line derived from a severely affected JBTS patient (NG2266) carrying two
184 pathogenic variants in the *RPGRIP1L* gene (p.Q684X/c.2304+1G>T) [50] **(Fig. 1B)**. Both variants
185 of this patient are predicted by VarSome to be null variants and are classified as pathogenic
186 following the pathogenicity criterium "very strong" (PVS1) accordingly to the ACMG
187 (American College of Medical Genetics and Genomics) standards and guidelines [51] and encode
188 truncated proteins missing the second C2 domain and C-terminal RPGR-Interacting domain
189 (RID) of the protein (see Methods and **Supplementary Fig. 5**). We generated cerebellar
190 organoids from both *RPGRIP1L* KO hiPSC lines (Ph2 and Wtc11) in parallel with their isogenic
191 controls, and from the JBTS patient-derived hiPSC line (NG2266).
192 Using a specific antibody raised against the human RPGRIP1L RID domain, we showed the
193 presence of RPGRIP1L protein at its subcellular localization at the ciliary transition zone in

194 control organoids (**Supplementary Fig. 2A, A'**). On the contrary, no signal was detected in cilia
195 from both *RPGRIP1L* KO and JBTS patient-derived organoids (**Supplementary Fig. 2B-C'**).
196 Bulk RNAseq analysis was performed on hiPSC cells and on cerebellar organoids collected
197 every seven days from day 7 to day 35 from several independent experiments (see
198 **Supplementary Excel File 1** for normalized gene expression data). We showed that both
199 *RPGRIP1L* KO and JBTS patient-derived organoids at day 7 expressed mid-hindbrain markers,
200 while being negative for anterior forebrain and caudal hindbrain markers **(Fig 1C),** thus
201 showing proper specification of their early anteroposterior identity. However, JBTS patient-
202 derived organoids displayed lower levels of WNT1 and EN1 than controls (**Fig. 1C**).
203 From day 14 onwards, transcriptome analysis revealed a consistent and severe reduction of
204 numerous Purkinje markers (*OLIG2, SKOR2, CALB1, FOXP2, PDE1C, ITPR1*) in both *RPGRIP1L*
205 KO and JBTS patient-derived organoids compared to controls **(Fig. 1D, Supplementary Fig. 2D)**.
206 Quantitative PCR analysis corroborated these results showing a significant decrease of *OLIG2,*
207 *SKOR2* and *CALB1* markers in *RPGRIP1L* KO organoids derived from both hiPSC lines and in
208 JBTS patient-derived organoids, compared to controls **(Supplementary Fig. 2E)**.
209 In contrast, the expression levels of the glutamatergic lineage markers *ATOH1* and *BARHL1*
210 were not consistently affected across *RPGRIP1L*-deficient conditions compared to controls
211 **(Figure 1E)**. This was confirmed by quantitative PCR analysis where the only significant defects
212 were a decrease in *BARHL1* expression in JBTS patient-derived organoids and an increase in
213 ATOH1 expression in *RPGRIP1L* KO organoids at d35 **(Supplementary Fig. 2F**).
214 In order to strengthen these findings, we assayed protein expression of both Purkinje lineage
215 markers (OLIG2, CALB1) and glutamatergic lineage markers (ATOH1, BARHL1) by quantifying
216 the number of positive cells after immunostaining on organoid cryosections. Each marker was
217 analyzed at the timepoint of its highest expression in control organoids, as determined by bulk
218 RNA-seq data: day 21 for OLIG2 and day 28 for CALB1, ATOH1, and BARHL1. OLIG2- and CALB1-
219 positive cells were barely detected in *RPGRIP1L* KO and JBTS patient-derived organoids, while
220 strong and widespread labeling was observed in control organoids (**Fig. 1F-I, Supplementary**
221 **Fig. 2I**). Regarding the glutamatergic lineage, the number of BARHL1 positive cells was reduced
222 by 50% in *RPGRIP1L* KO and JBTS patient-derived organoids, along with a decrease in the
223 average labeling intensity of individual cells (**Fig. 1J, K, Supplementary Fig. 2J**). The number of
224 ATOH1 positive cells was only reduced in JBTS patient organoids (**Supplementary Fig. 2G, H)**

225 whereas the intensity of ATOH1 labelling was reduced by ~50% both in JBTS patient and
226 *RPGRIP1L* KO conditions (**Supplementary Fig. 2K**).
227 Overall, these data indicate a severe and significant impairment in the specification and
228 production of the Purkinje lineage in all *RPGRIP1L*-deficient conditions from day 21 onwards,
229 whereas glutamatergic lineage specification appeared to be modestly affected, mainly at
230 protein level from day 28.
231
232 ***Increased proportion of early neural progenitors in RPGRIP1L KO and JBTS patient cerebellar***
233 ***organoids***
234 We assessed whether these molecular alterations observed upon *RPGRIP1L* impairment might
235 be preceded by earlier defects in tissue organization. The first obvious morphological
236 alteration under brightfield observation was a size increase of *RPGRIP1L* KO and JBTS patient
237 organoids compared to controls, from day 21 onward **(Fig. 2A)**. Organoid area was measured
238 every 7 days along the differentiation protocol in several independent experiments. At day 28
239 and 35, both *RPGRIP1L* KO and JBTS patient-derived organoids presented a significant area
240 increase compared to controls (3.3-fold for *RPGRIP1L* KO and 2.3-fold for JBTS patient-derived
241 organoids over controls at day 35) **(Fig. 2B)**.
242 Moreover, the general tissue organization was already perturbed at day 14, before overt size
243 increase. In control organoids, early polarized neural progenitors ($SOX2^+/ZO1^+$) formed few
244 internal rosettes **(Fig. 2C left panels)**. By contrast, *RPGRIP1L* KO (Ph2 and Wtc11 lines) and
245 JBTS patient-derived organoids exhibited a higher number of internal rosettes. Additionally, in
246 all *RPGRIP1L*-deficient conditions, polarized neural progenitors ($SOX2^+/ZO1^+$) extended across
247 the entire organoid surface, with their apical side oriented outward, forming a continuous
248 neuroepithelium in contact with the medium **(Fig. 2C, middle and right panels)**.
249 The area occupied by ZO1 apical surface within the organoid was expanded by 12-fold in
250 *RPGRIP1L*-KO (Ph2 and Wtc11 lines) and by 15-fold in JBTS patient-derived organoids
251 compared to control condition at day 14 **(Fig. 2D).** Similarly, the number of SOX2+ neural
252 progenitors was doubled in all *RPGRIP1L*-deficient conditions compared to controls **(Fig. 2E)**.
253
254 ***Differential dependence on RPGRIP1L protein among neural progenitors for ciliogenesis***
255 Given the well-established role of *RPGRIP1L* in building functional cilia [21,52,22] and the fact that
256 apical progenitors of the neural tube are ciliated [53–56], we investigated whether ciliogenesis

257 was affected in human cerebellar organoids. Immunostaining for the axonemal marker INPP5E
258 and for the basal body marker gamma-TUBULIN revealed numerous cilia pointing towards the
259 internal lumen of neural rosettes in both controls **(Fig. 3A, A')** and all *RPGRIP1L*-deficient
260 conditions **(Fig. 3B-C')**. Some cilia in *RPGRIP1L* KO and JBTS rosettes displayed a bulbous tip
261 **(Fig. 3B', C')**, a condition which was never observed in control rosettes. However, ciliary length
262 was not significantly changed in *RPGRIP1L* KO rosettes and only mildly decreased in JBTS
263 condition **(Fig. 3D)**.
264 In contrast, the analysis of non-polarized regions, characterized by random nuclear orientation
265 and distribution of gamma-TUBULIN+ basal bodies **(Fig. 3E-G)**, revealed a nearly two-fold
266 reduction in the number of cilia in *RPGRIP1L*-KO and JBTS patient organoids (48% in *RPGRIP1L*-
267 KO, 42% in JBTS-severe, versus 84% of mean percentage of ciliation in controls) **(Fig. 3H).**
268 Moreover, INPP5E labeling intensity inside cilia was reduced **(Fig. 3I)** and ciliary length
269 increased **(Fig. 3J)**. Altogether these results indicate an impaired ciliogenesis and altered
270 ciliary trafficking in *RPGRIP1L*-depleted non-polarized cells. Consistent with the literature
271 indicating a cell type-specific requirement for *RPGRIP1L* at the ciliary transition zone [52], our
272 findings suggest that, in cerebellar organoids, *RPGRIP1L* is necessary for both proper
273 ciliogenesis and ciliary content in non-polarized neural progenitors, while it appears
274 dispensable for ciliogenesis in $ZO1^+$ early human cerebellar progenitors at day 14.
275 Nevertheless, the observation of numerous bulbous tips on cilia of apical progenitors suggests
276 that they might present an abnormal content, likely to modify their signaling properties.
277
278 ***FGF signaling upregulation and neurogenesis impairment in RPGRIP1L-deficient cerebellar***
279 ***organoids***
280 In order to identify specific molecular pathways disrupted upon RPGRIP1L depletion we
281 performed a DESeq2 analysis on our bulk RNAseq dataset, comparing both *RPGRIP1L* KO and
282 JBTS patient-derived organoids with controls at selected timepoints.
283 At day 14, many genes appeared deregulated in both *RPGRIP1L* KO (2146 genes, P adj <0.05,
284 |log2FC|>1) and JBTS patient-derived organoids (4304 genes, P value <0.05, |log2FC|>1)
285 compared to controls (**Supplementary Excel Files 2 and 3,** respectively). The Volcano plots
286 representing significant DEGs (P value <0.05, |log2FC|>1) for *RPGRIP1L* KO compared to
287 control **(Fig. 4A)** or JBTS patient compared to control **(Fig. 4B)** revealed many genes commonly
288 de-regulated in both RPGRIP1L-deficient conditions. Most importantly, FGF signaling emerged

289 as a severely disrupted pathway, with many FGF ligands (FGF8, FGF19, FGF17) and direct
290 downstream targets (ETV4, ETV5, SPRY1-2-4) strongly up-regulated in both *RPGRIP1L* KO and
291 JBTS patient-derived organoids. In particular, FGF8 emerged as the top up-regulated FGF
292 ligand gene, with a peak of maximal over-expression at day 14 in *RPGRIP1L* KO organoids
293 (log2FC=4.07, p adj=7.10E-30) and JBTS patient organoids (log2FC=6.01, p adj=3.24E-32). Real-
294 time quantitative PCR analysis of FGF8 expression confirmed this up-regulation between day
295 14 and day 21 in *RPGRIP1L* KO and JBTS patient conditions versus controls and a more
296 exacerbate phenotype in JBTS patient organoids **(Fig. 4C).** Several *SOX* and *HES* transcription
297 factors, important to maintain a neural progenitor state, were also significantly up-regulated
298 in both *RPGRIP1L* KO and JBTS patient-derived organoids compared to controls (**Fig. 4A, B**).
299 On the contrary, neurogenic master genes – *NEUROG1*, *NEUROD1* and *NEUROD4* – were
300 severely down-regulated as well as other genes involved in neurogenesis and early-born
301 neuron functions like *HES6* [57,58], *GDNF* and *RELN* (**Fig. 4A, B**). To illustrate the reproducibility
302 of the differentiation protocol as well as the similarity of transcriptional changes between
303 *RPGRIP1L* KO and JBTS patient-derived organoids, we generated a heatmap representation of
304 normalized RNA expression values for selected genes over time **(Fig. 4D)**. While in control
305 samples, FGF signaling peaked at day 7 and was turned off by day 14, in both *RPGRIP1L* KO
306 and JBTS patient-derived organoids this signaling was upregulated and longer maintained
307 (until day 21). Overall, these data suggest that the failure to down-regulate FGF signaling after
308 midbrain-hindbrain boundary specification in *RPGRIP1L*-deficient conditions may prevent
309 neurogenesis by maintaining early neural cells in their progenitor state.
310 To better characterize the massive upregulation of FGF signaling, we thus assessed which cells
311 were producing the FGF8 protein. Immunostaining analysis on cryosections of day 14
312 organoids revealed that the strongest FGF8 signal coincided with the apical surfaces of early
313 $SOX2^+/ZO1^+$ apical progenitors (**Supplementary Fig. 3**). In control organoids we could only
314 detect signal in cells bordering the few internal lumens (**Supplementary Fig. 3A, D).** In
315 *RPGRIP1L* KO and JBTS patient-derived organoids, FGF8 distribution was more widespread.
316 Indeed, FGF8 was enriched on both the apical sides of neural progenitors forming internal
317 lumens (**Supplementary Fig. 3B, C, E, F)** and the external layer covering the organoid surface
318 (**Supplementary Fig. 3B, C, G, H)**. The overall increase of *FGF8* mRNA levels observed in
319 *RPGRIP1L* KO and JBTS patient-derived organoids is consistent with the increased number of
320 $SOX2^+/ZO1^+$ progenitors.

321

322 ***RPGRIP1L-deficient organoids display severe neuronal maturation and extracellular matrix***
323 ***defects***

324 To assess whether the impaired neurogenesis observed at early differentiation stages (day 14)
325 prevented the acquisition of a mature neuronal signature in *RPGRIP1L*-deficient conditions,
326 we analyzed DEG's profile at later stages. At day 28, we observed a significant downregulation
327 of numerous genes involved in neuronal maturation and function, both in *RPGRIP1L* KO and
328 JBTS patient conditions (**Supplementary Excel Files 4 and 5,** respectively) as illustrated by the
329 volcano plots **(Fig. 5A, B**) and on the heatmap representation of normalized RNA expression
330 values over time (**Fig. 5C, upper panel**). In absence of functional RPGRIP1L protein we also
331 observed a severe reduction of several genes encoding extracellular-matrix (ECM)
332 components, such as collagens and laminins, as well as integrin receptors **(Fig. 5A, B and Fig.**
333 **5C lower panel)**.

334 Gene ontology analyses performed to identify overrepresented gene categories in our DEG
335 lists corroborated these results. Indeed, the most significantly enriched GO terms among the
336 downregulated genes in both *RPGRIP1L* KO (**Fig 5D**) and JBTS patient (**Fig 5E**) conditions at day
337 28 included brain development, synaptic signaling/chemical synaptic transmission, regulation
338 of membrane potential/action potential, but also core matrisome and extracellular matrix
339 organization.

340 Altogether these results demonstrated a neuronal maturation impairment, following FGF
341 upregulation and neurogenesis defects at early stages, and highlighted a concomitant
342 transcriptional downregulation of major ECM components.

343

344 ***Blocking FGF signaling rescues neurogenesis and Purkinje cell progenitors in RPGRIP1L-***
345 ***deficient cerebellar organoids***

346 To test the hypothesis that the sustained and strong FGF signaling upon *RPGRIP1L* depletion
347 is at the origin of neurogenesis and neuronal differentiation impairment, we designed a drug
348 rescue experiment. Given that FGF8 expression is crucial for midbrain-hindbrain boundary
349 formation at early stages and that, in *RPGRIP1L*-deficient organoids, the over-expression of
350 FGF ligands and of their downstream targets started before day 14 and continued until day
351 21, we treated *RPGRIP1L*-deficient organoids (both KO and JBTS patient lines) with the pan-
352 FGFR inhibitor BGJ-398 (Infigratinib), from day 11 to day 18 (**Supplementary Fig. 4A**). Notably,

353 BGJ-398 treatment restored a normal size of *RPGRIP1L*-KO and JBTS patient organoids
354 (**Supplementary Fig. 4B**).
355 We then performed bulk RNAseq analysis on the BGJ treated samples and compared them to
356 their untreated counterparts. Heatmap representation of normalized RNA expression values
357 for selected genes over time clearly show that BGJ treatment was able to rescue defects of
358 FGF signaling, as well as neurogenesis, neuronal differentiation and extracellular matrix
359 production in both RPGRIP1L KO **(Fig. 6A)** and JBTS patient organoids **(Fig. 6B)** from several
360 independent experiments (see **Supplementary Excel File 6** for normalized gene expression
361 data)**.**
362 Quantitative PCR analysis confirmed these results: the RNA expression levels of *FGF8* and its
363 downstream targets (*ETV4, ETV5, SPRY1*) were completely restored by the drug treatment in
364 both RPGRIP1L KO and JBTS patient organoids at all timepoints analyzed **(Supplementary Fig.**
365 **4E-H)**. The expression levels of proneural genes *NEUROG1* and *NEUROD1*, as well as Purkinje
366 markers *SKOR2* and *CALB1*, analyzed by quantitative PCR were partially rescued in *RPGRIP1L*
367 KO and JBTS patient organoids upon BGJ-398 treatment, in particular at their peak of
368 expression (**Supplementary Fig. 4I-L**). Immunofluorescence analysis on cryosections of day 14
369 organoids corroborated these results, showing a significant rescue in the number of positive
370 nuclei for either NEUROD1, HUC/D or SOX2 markers, upon BGJ-398 treatment in both
371 *RPGRIP1L* KO or JBTS patient-derived organoids (**Fig. 6C-F**). The expression level of the Purkinje
372 progenitor marker OLIG2 was also significantly rescued upon BGJ-398 treatment in both
373 *RPGRIP1L* KO and JBTS patient-derived organoids, as shown by immunofluorescence analysis
374 at day 21 **(Fig. 6G, H)**.
375 Thus, downregulating FGF signaling efficiently rescued the neurogenesis defect in *RPGRIP1L*-
376 deficient cerebellar organoids as well as the production of Purkinje cell progenitors.
377
378 ***Neural progenitor proliferation is increased in RPGRIP1L-deficient organoids and is rescued***
379 ***by blocking FGF signaling***
380 To test whether the size increase observed upon *RPGRIP1L* impairment could be due to
381 sustained proliferation caused by FGF overexpression, we assessed the proliferative potential
382 of neural progenitors in control, *RPGRIP1L* KO and JBTS patient-derived organoids by carrying
383 EdU pulse-chase experiments. We provided a 2h EdU pulse to the organoid cultures at day 18,
384 just before the onset of size increase. Some organoids were fixed 2h after the pulse. At this

385 stage (day 18), all *RPGRIP1L*-deficient organoids showed an increase of EdU positive cells
386 compared to controls (1.6-fold in *RPGRIP1L* KO, 2.6-fold in JBTS patient). BGJ-398 treatment
387 significantly reduced the number of EdU-incorporating cells in *RPGRIP1L* KO but not in JBTS
388 patient-derived organoids (**Fig. 7A, B**). Of note, similar results were obtained whether
389 considering the number of double $EdU^+/SOX2^+$ cells among the population of $SOX2^+$ cells,
390 indicating more progenitors in S-phase (**Fig. 7C**).
391 A chase assay was performed by removing EdU from the medium after 2 hours and fixing
392 organoids five days after the EdU pulse (i.e. day 23). The number of EdU Label Retaining Cells
393 (LRCs) was strongly reduced in both *RPGRIP1L* KO and JBTS patient conditions compared to
394 controls (~2-fold decrease) **(Fig. 7D, E)**. This indicates that, in the time-window analyzed
395 (between day 18 and day 23), *RPGRIP1L* KO and JBTS patient-derived cells proliferated more
396 than controls, leading to the dilution of most EdU labeling. BGJ-398 treatment significantly
397 restored the number of LRCs in both *RPGRIP1L* KO and JBTS patient-derived organoids **(Fig.
398 7D, E)**. EdU co-labeling with the progenitor marker SOX2 and the quantification of double
399 $EdU^+/SOX2^+$ cells among the $SOX2^+$ population showed similar results (**Fig. 7F**).
400 In addition, when dividing EdU+ cells into two categories—"strong" and "faint"—based on
401 labeling intensity, we observed that the "strong" EdU+ population, likely representing cells
402 that underwent at most one division after EdU incorporation, was the most affected in both
403 *RPGRIP1L*-deficient conditions and restored by BGJ-398 treatment **(Fig. 7G)**. Overall, FGF
404 overactivation in *RPGRIP1L*-deficient cerebellar organoids maintains SOX2+ progenitors in a
405 proliferative state and prevents their switch to neuronal differentiation and maturation,
406 reducing drastically Purkinje cell formation.
407
408 **DISCUSSION**
409
410 A crucial role of primary cilia for proper cerebellar development has been identified in mouse
411 mutants for ciliary genes, which present varying degrees of cerebellar hypoplasia [30–35].
412 However, the mechanisms linking mutations in ciliary genes to human cerebellar impairment,
413 as well as the developmental origin of specific JBTS patient cerebellar features, remain largely
414 unknown. Importantly, critical aspects of this disease may be missed in mouse models, as
415 cerebellar formation in humans presents unique features [9,10,59], and JBTS genes dysfunction
416 does not necessarily impact ciliogenesis the same way in both species [45]. To overcome this

417 issue, in this study we leveraged human cerebellar organoids to investigate the formation of
418 early cerebellar progenitors under healthy and pathological conditions linked to mutations in
419 *RPGRIP1L*, a JBTS causal gene. Our study uncovered an increased proliferation of neural
420 progenitors and a reduction of neurogenesis and Purkinje cell production in *RPGRIP1L*-
421 deficient cerebellar organoids. These defects are correlated with strong FGF pathway
422 upregulation. Rescue experiments by blocking FGF receptors (FGFRs) demonstrate the causal
423 link of FGF up-regulation with neurogenesis-proliferation imbalance and with the reduction of
424 Purkinje cell formation.
425
426 Given the important role of RPGRIP1L for ciliary functions, we analyzed cilia formation and
427 ciliary content in *RPGRIP1L*-deficient cerebellar organoids compared to controls. We showed
428 that the RPGRIP1L protein is differentially required for ciliogenesis in early neural progenitors,
429 since its loss causes severe ciliary defects in non-polarized progenitors, while mild
430 morphological defects are observed in polarized apical progenitors. This difference may result
431 from variations in ciliogenesis pathways and reinforces existing literature indicating a cell type-
432 specific requirement for RPGRIP1L at the ciliary transition zone. Indeed, studies in mice have
433 demonstrated that, in specific cell types, compensatory mechanism involving the RPGRIP1L
434 paralogue – RPGRIP1 – could overcome RPGRIP1L depletion [52]. Moreover, in depth analysis of
435 cilia distribution and morphology in the mouse cerebral cortex and cerebellum challenged the
436 traditional view that cilia are uniformly present and identical in all brain regions and cell types
437 [60,61,27], a variability that may, at least partially, contribute to the differential vulnerability of
438 brain regions to mutations in ciliary genes. A reduced number of cilia on non-polarized cells
439 could either result from decreased ciliogenesis, or increased ciliary instability/disassembly.
440 Anyhow, this reduction is unlikely to be a consequence of the FGF pathway up-regulation, as
441 FGF signaling has been shown to promote ciliogenesis [62,63] rather than inhibiting it.
442
443 Our data suggest that defects in RPGRIP1L-deficient cerebellar organoids appear after the
444 initial cerebellum induction stages: while midbrain-hindbrain boundary markers were
445 expressed at day 7 in all genotype conditions, temporal expression analysis of typical
446 cerebellar cell markers revealed a strong reduction of all analyzed markers of the Purkinje
447 lineage, from day 21 to 35. Whether this reflects a defect in Purkinje cell specification and/or
448 in their differentiation remains to be determined. Purkinje cells being early-born neurons in

449 the human cerebellum (8-10 PCW) [8,9], the strong defect in their production in *RPGRIP1L*-
450 deficient organoids might stem from the general neurogenesis defect. Indeed, the concurrent
451 rescue of neurogenesis and expression of the Purkinje markers OLIG2, SKOR2 and CALB1
452 following FGFR inhibitor treatment strongly suggests that the two defects are linked. The GCP
453 population appears less affected when considering GCP marker RNA levels. However, we did
454 observe a 50% reduction in the number and staining intensity of BARHL1-expressing cells at
455 day 28, suggesting that the glutamatergic lineage might also be affected at later stages,
456 consistent with the late maturation of GNs in humans [9,48]. Transcriptome analysis also
457 revealed a severe downregulation of several integrins and ECM components, perturbing the
458 ECM-receptor system in *RPGRIP1L*-deficient organoids. Although the causes of this alteration
459 are unclear, it might participate in the neurogenesis and neuronal maturation impairment in
460 *RPGRIP1L*-deficient organoids. Indeed, the expression of ECM molecules is dynamically
461 regulated during brain development and plays prominent roles in neurogenesis, cell
462 migration, neurite outgrowth and synaptogenesis [64–66].
463
464 FGF8 is known as the key morphogen to establish early cerebellar territory *in vivo* [67]. Notably,
465 the dose, the precise location and the time window of FGF8 expression need to be tightly
466 controlled to allow proper cerebellar development [68]. Ectopically upregulating *Fgf8* in
467 cerebellar precursors increases their proliferation and overrides their normal program of cell
468 specification [69]. Moreover, conditional inactivation in the mouse isthmus of *Sprouty* genes
469 (*Spry1-2-4*), which are FGF direct targets acting as feedback loop negative regulators [70], results
470 in overactivation of FGF signaling and aberrant cerebellar development [71]. A growing literature
471 emphasizes the role of the FGF pathway in regulating the proliferative/neurogenic balance in
472 early neural development, by promoting progenitor proliferation at the expense of neuronal
473 differentiation during embryonic spinal cord elongation [72–74] and corticogenesis [75,76].
474 Interestingly, the development of the vermis in mice relies on a higher and longer FGF8 dosage
475 than the hemispheres [68,77]. During early developmental stages, the region expressing FGF8
476 corresponds to the prospective vermis [78], which has been identified as a direct derivative of
477 these FGF8-expressing isthmic cells [79].
478 In our cerebellar differentiation protocol, control organoids downregulated *FGF8* after day 7,
479 while *RPGRIP1L*-deficient organoids displayed a massive FGF8 up-regulation from day 14 to
480 21. Consistent with current literature, we showed that the increased levels of FGF ligands

481 (*FGF8, FGF17, FGF19*) and pathway activation, as indicated by the expression of *ETV*4-5 target
482 genes, were responsible for the impaired neurogenesis and neuronal differentiation observed
483 upon *RPGRIP1L* depletion.
484 Which mechanisms could underlie FGF upregulation upon *RPGRIP1L*-deficiency remains an
485 open question. We revealed the presence of FGF8 protein mainly in apical neural progenitors,
486 suggesting that they are the FGF8 producing cells. It is difficult to establish whether the
487 increased number of apical progenitors is the initial cause or the consequence of higher FGF
488 production in RPGRIP1L-deficient conditions. Nevertheless, we provided evidence that, once
489 engaged, this mechanism could be self-sustaining, with FGF signaling promoting progenitor
490 proliferation. Alternatively, SP8 transcription factor, a well-known inducer and target of FGF8
491 [80–82], could participate in a self-amplification loop, being significantly upregulated in all
492 *RPGRIP1L*-deficient conditions at both day 14 and 21 (see DEGs tables).
493
494 An essential question raised by our study is the link between the early increased proliferation
495 observed in cerebellar organoids and the vermis hypoplasia found in JBTS patients. Although
496 we cannot exclude that the context of organoids could favor specific manifestations of the
497 *RPGRIP1L* mutant phenotype that are not revealed *in vivo*, several hypotheses could explain
498 these apparently opposite phenotypes. First, an early over-proliferation could trigger later cell
499 death. As an example, widespread apoptosis was observed after over-proliferation upon loss
500 of function of the kinase DYRK1A [83] and was interpreted as a consequence of uncoupling cell
501 cycle exit from neuronal differentiation. Another possibility would be that an increase in early
502 progenitor numbers would preferentially populate the cerebellar hemispheres at the expense
503 of the vermis. Indeed, lineage studies in mice highlight different medio-lateral distribution of
504 cerebellar VZ clones according to their birth dates [84,85]. Finally, an expansion of the midbrain-
505 hindbrain boundary signaling center due to FGF8 overexpression could impair morphogenetic
506 movements leading to midline fusion of the bilateral cerebellar primordia and thus vermis
507 formation, as shown in chicken embryos [86]. These morphogenetic movements do not happen
508 in organoids but could explain the vermis hypoplasia in ciliopathy patients. The long-term
509 consequences of impaired differentiation and sustained proliferation in cerebellar organoids
510 will have to be investigated.
511 Whatever the mechanism, increased proliferation in cerebellar organoids is consistent with
512 data obtained in mouse mutants for two JBTS causal genes, KIF17 [87] and SUFU. The case of

513 SUFU, a negative regulator of the HH pathway that acts at the cilium, is particularly striking.
514 In mice, conditional invalidation of SUFU in GCPs or Purkinje progenitors leads to protracted
515 proliferation and delayed differentiation, as well as to FGF8 pathway upregulation in cerebellar
516 progenitors [88–90]. Notably, early SUFU invalidation in the cerebellar anlage leads to loss of the
517 vermis [89], mimicking a ciliopathy phenotype. In humans, germline SUFU haploinsufficiency or
518 recessive hypomorphic mutations in SUFU can be associated with mild forms of JBTS
519 encompassing cerebellar vermis hypoplasia [91,92]. On the other hand, germline SUFU
520 haploinsufficiency is also a strong risk factor for the development of severe infantile
521 medulloblastoma (of SHH-MB class) [93,94]. Additionally, some SUFU variants have been
522 reported both in JBTS and cancer [92]. This, together with our data on *RPGRIP1L* deficiency in
523 cerebellar organoids, raises the puzzling question of potential common mechanisms between
524 early cerebellar progenitor hyperproliferation and later vermis hypoplasia.
525
526 The relevance of our study for JBTS pathology is emphasized by the similar phenotypes of
527 *RPGRIP1L* KO organoids with organoids derived from a JBTS patient's iPSC line. The JBTS
528 patient donor of the NG2266 cell line used in this study, exhibits a very severe neurological
529 phenotype, correlated with vermis hypoplasia and partial aplasia, as revealed by encephalic
530 magnetic resonance imaging (MRI). The patient carries two biallelic heterozygous mutations
531 in the *RPGRIP1L* gene: a nonsense mutation at the end of the first C2 protein domain, and a
532 splice variant that results in the generation of a stop codon at the beginning of the second C2
533 domain. Given the importance of both C2 domains for RPGRIP1L function [95,96,30,97,21], a stop
534 codon in these domains is likely to impair protein functionality. Indeed, similar to the
535 *RPGRIP1L* KO condition, JBTS patient (NG2266)-derived organoids lacked RPGRIP1L protein at
536 the ciliary transition zone. This further underscores the strong phenotypical similarity
537 observed between *RPGRIP1L* KO and JBTS patient (NG2266)-derived organoids. Furthermore,
538 targeted pharmacological inhibition of FGFR using BGJ-398/Infigratinib, an FDA-approved drug
539 currently used in oncology and to treat hypochondroplasia [98], is sufficient to rescue the
540 proliferative-neurogenic balance and to restore Purkinje cell lineage formation, both in
541 *RPGRIP1L* knockout hiPSC lines and in the Joubert syndrome patient line, establishing a
542 mechanistic link between FGF overactivation and the observed phenotypical alterations.
543

544 More generally, it will be crucial to determine whether the molecular alterations reported in
545 this study have broader relevance by also occurring in cerebellar organoids with mutations in
546 other JBTS genes, or if they are specific to *RPGRIP1L* depletion. Indeed, not all JBTS patients
547 present cerebellar vermis hypoplasia; in milder cases, the cerebellar vermis may be dysplastic
548 without a reduction in size [99]. It will be particularly helpful to investigate whether FGF signaling
549 could be specifically disrupted in cerebellar organoids from patients with severe vermis
550 hypoplasia, as it might be of predictive value for the severity of the neurological phenotype.
551
552 In conclusion, with this work we provide an example of a cerebellar organoid approach to
553 investigate potential pathogenetic mechanisms underlying a human disease. Our results
554 uncover unexpected defects in neurogenesis linked to increased FGF signaling, thereby
555 offering a novel framework for investigating the etiology of cerebellar defects in JBTS and
556 other neurodevelopmental diseases.
557
558
559 **MATERIAL AND METHODS**
560
561 **Ethics**
562 The work performed in this manuscript complies with all relevant ethical regulations. The
563 obtaining and manipulation of human iPSC lines were performed under ethical agreements
564 from the French Ministry of Higher Education and Research DC-2025-7003 (for the UCSFi001-
565 A and PCIi033-A lines, control and RPGRIP1L-KO) and DC-2025-7496 (for the JBTS patient line)
566 and under GMO authorization number DUO-9509.
567
568 **hiPSC culture**
569 hiPSCs were thawed in mTeSR+ medium (Stem Cell Technologies #100-0276) in the presence
570 of Rock-inhibitor Y-27632 (5µM, Stemgent-Ozyme #04-0012) and cultured on Matrigel
571 (Corning, VWR #354277) coated plates under standard conditions at 37°C upon confluency of
572 70-80%. The medium was changed every two days. Passaging was performed using ReLeSR
573 (Stem Cell Technologies #05872) and testing for potential mycoplasma contamination was
574 performed regularly by Eurofins genomic (Mycoplasmacheck). Accutase (Stem Cell

575 Technologies #07920) was used for the dissociation of hiPSC colonies into single cells prior to
576 the differentiation protocol.
577
578 **Clinical features of the patient COR201 and characterization of the mutant Identification of**
579 **the RPGRIP1L RNA products derived from the NG2266 hiPSC c.2304+1G>T splice variant**
580 **allele.**
581 The NG2266 cell line is derived from the male patient COR201 [50] who was last examined at
582 the age of 17. He presented a molar tooth sign on brain MRI and his neurological examination
583 revealed hypotonia, psychomotor delay, neonatal breathing dysregulation, ocular-motor
584 apraxia, nystagmus and severe intellectual disability. Post-axial polydactyly of the left hand
585 was present at birth. During evolution, he suffered severe visual impairment and strabismus,
586 severe renal dysfunction (chronic renal failure at the age of 11, which required renal
587 transplantation at age 14), as well as chronic liver disease.
588 We demonstrated by sequencing PCR products from NG2266 hiPSCs cDNA that the splice
589 variant c.2304+1G>T resulted in intron retention leading to an early stop codon at position
590 788 (S788X). Primer 1 (Forward: GTATCCATAAACTAGAAGCCCAAT) was designed at the junction
591 between exon 14 and 15; primer 2 (Reverse: GGGTTAAGGTTACAGGGGATCTC) was placed in
592 the intron between exon 16 and 17; Primer 3 (Reverse: AATATTCCTGAGATACACCTGTC) was
593 positioned at the junction between exon 17 and 18 **(Supplementary Fig. 5A)**. PCR products
594 were analyzed on agarose gel and showed that primer pair 1-2 amplified an 813 bp region in
595 the cDNA derived from JBTS patient (NG2266) hiPSCs but not from the control condition
596 **(Supplementary Fig. 5B)**. Primer pair 1-3 amplified a 1009 bp region, both in the control and
597 in JBTS patient cDNA. As expected, NG2266 second allele (c.2050C>T/p.Q684X) presents a
598 nonsense mutation that does not affect the cDNA structure, resulting in a PCR product of the
599 same size as control alleles. On the contrary, using the primer pair 1-3, the c.2304+1G>T allele
600 could not be amplified from cDNA given that intron retention would give rise to a 3969 bp PCR
601 product **(Supplementary Fig. 5B')**.
602 Primer pair 1-2 PCR product from NG2266 hiPSCs was sequenced to confirm the intron
603 retention. An ATG stop codon appear 29 nt after the beginning of the intron sequence, most
604 likely giving rise to a truncated form of the protein **(Supplementary Fig. 5C)**.
605 Moreover, an additional mutation was identified in the exon 16: c.2231 G>A (p. R744Q).
606

607 **Differentiation of hiPSCs into cerebellar organoids**

608 After two amplification passages, hiPSC lines (characterized in [50,52]) were dissociated into
609 single cells using Accutase (Stem Cell Technologies #07920) and resuspended in mTeSR+
610 medium supplemented with 10 µM ROCK inhibitor. Then, cells were promptly re-aggregated
611 using AggreWell™800 microwell plates (StemCell Technologies) following the manufacturer's
612 instructions. Cells were seeded at a density of 1.8 × 10^6 cells per well (6,000 cells per
613 microwell). This corresponded to day 0 of the cerebellar differentiation protocol. Two days
614 later the entire medium was replaced with the chemically defined medium (gfCDM), slightly
615 modified compared to [37], consisting of vol:vol Isocove's modified Dulbecco's medium (Thermo
616 Fisher #12440053)/Advanced DMEM/F-12 (Thermo Fisher #12634028), chemically defined
617 lipid concentrate (1% v/v, Thermo Fisher #11905031), monothioglycerol (450 µM, Sigma
618 #M6154), apo-transferrin (15 µg/ml, Sigma #T1147), crystallization-purified BSA (5 mg/ml,
619 >99%, Sigma #5470), and 50 U/ml penicillin/50 µg/ml streptomycin (P/S, Thermo Fisher
620 #15140122). The medium was also supplemented with insulin (7 µg/ml, Sigma #I9278) and
621 used from day 2 to day 21. Different factors were added to the medium at different timepoints
622 as represented in Fig. 1A. Recombinant human basic FGF (FGF2, 50 ng/ml, PeproTech # 100-
623 18B) and SB431542 (SB, 10 µM, Stemgent-Ozyme #04-0010) were added to the culture on day
624 2. On day 4, floating aggregates were transferred from microwell plates to ultra-low
625 attachment dishes (Corning #3261) and total medium change with drug refreshment was
626 performed. On day 7 embryoid bodies(EBs)-containing dishes were transferred to an orbital
627 shaker (3 mm orbit, Thermo Scientific #88881102B) and maintained under orbital agitation of
628 100 rpm until the end of the protocol. Total medium change with 2/3 of the initial amount of
629 FGF2 and SB431542 was performed on day 7, day 9 and day 11. On day 14, FGF2 and SB431542
630 were replaced by medium change supplemented with recombinant FGF19 (100 ng/ml;
631 PeproTech #100-32). The same medium change was also performed at day 16 and 18. From
632 day 21 onward, the aggregates were cultured in Neurobasal medium (Thermo Fisher
633 #21103049) supplemented with GlutaMax I (Thermo Fisher #35050061), N2 supplement
634 (Thermo Fisher #17502048), and P/S 1% (Thermo Fisher #15140122). Total medium changes
635 were performed on day 23, 25, 28, 30 and 32. Recombinant human SDF1 (300 ng/ml,
636 PeproTech #300-28A) was added to the culture from day 28 onward (**Fig. 1A**). For pan-FGFR
637 inhibition, BGJ-398/Infigratinib was first added at day 11 at a concentration of 100 nM and

638 renewed on days 14 and 16. At day 18 total medium was replaced by fresh medium devoid of
639 BGJ-398.
640
641 **EdU treatment and labeling**
642 Cerebellar organoids at day 18 were incubated using 10 µM EdU (Click-iT EdU Imaging Kit,
643 Invitrogen) dissolved in growth medium for 2 h at 37 °C and then washed twice with PBS.
644 Around 30 organoids per genotype were collected and fixed for 20 minutes at room
645 temperature in 4% cold PFA. The remaining organoids, around 30 per genotype, were kept in
646 culture after washing for a 5-day chase until day 23 of the differentiation protocol, when they
647 were collected and fixed in the same way.
648 Fixed organoids were embedded in OCT following the procedure described in the section
649 Organoids embedding and Cryosectioning**.** EdU labeling detection on cryosections was
650 performed according to the Click-iT EdU Imaging Kit manufacturer's instruction at the end of
651 our immunostaining protocol (refer to the following section "Immunofluorescence").
652
653 **Organoid Size Analysis**
654 To monitor the organoid size, bright-field images were acquired at different time-points (every
655 seven days). Organoid area was calculated by manually dragging a line with the freehand
656 selections tool on Fiji (ImageJ; National Institutes of Health) and subsequently measuring the
657 object area. Organoid area was measured in several independent experiments (N=3 Ph2 line,
658 N=3 Wtc11 line, N=3 NG2266 line), n=10-60 organoids were analyzed per experiment per
659 condition. Results are presented as the mean ± SEM of organoid averages from each individual
660 experiment.
661
662 **Organoids embedding and Cryosectioning**
663 Organoids were collected every seven days during differentiation from day 7 to 35, rinsed with
664 PBS and fixed in cold PFA (4 %) for 20 min at 4 °C. Then organoids were rinsed in PBS and
665 incubated in 30 % sucrose in PBS until completely saturated. Cryoprotected organoids were
666 embedded in OCT matrix (Cell Path #KMA-0100-00A) in plastic molds and stored at -80 °C. 12
667 µM cryostat sections were prepared and stored at -20 °C.
668
669

670 **Immunofluorescence**

671 Cryostat sections of organoids were washed in PBS/0.1% Triton X-100. An optional step of
672 antigen-retrieval with Citrate-Buffer was performed only for cilia staining (INPP5E and
673 Gamma-TUBULIN antibodies). After washing, cryosections were incubated with a blocking
674 solution containing 10% NGS in PBS/0.1% Triton-X100 for at least 2 hours. The sections were
675 incubated overnight at 4 °C with primary antibodies **(Supplementary Table 5)** diluted in a
676 solution containing 1% NGS in PBS/0.1% Triton-X100. Next day, the slides were washed 3 x 10
677 min with PBS/0.1% Triton-X100 and incubated with secondary antibodies at 1:400 dilution
678 **(Supplementary Table 6)** and DAPI (Merck #1.24653) in 1% NGS/PBS/0.1 % Triton X-100 for 2
679 hours. After final washing steps with PBS/0.1 %Triton X-100 for at least 1 hour, sections were
680 mounted with Mowiol (Roth #0713.2).

681

682 **Image acquisition**

683 Fluorescence image acquisition of cerebellar progenitors and neuronal markers was
684 performed at room temperature using a Zeiss Observer Z1 equipped with an Apotome
685 module, an Axiocam 506 monochrome cooled CCD camera and a 20x objective. Z-stacks with
686 1 µM step were acquired. All images were processed with Zen software (blue edition). For cilia
687 analyses, fluorescence images were acquired at room temperature using a confocal
688 microscope (LSM 980 upright, Carl Zeiss AG) and a 63x oil objective with a NA 1.4 and a
689 monochrome charge-coupled device camera. Z-stacks with 0.25 µM step were acquired.
690 Images were processed with Zen software (black edition).

691

692 **Quantification of immunofluorescent staining and statistical analyses**

693 The number of positive cells in immunofluorescence staining was quantified on 7µm Z-
694 projections using the Cellpose environment
695 (https://cellpose.readthedocs.io/en/latest/installation.html) for cell segmentation. Each
696 image was segmented using the DAPI channel to generate a mask identifying all nuclei. The
697 intensity of the target channel was then measured for each nucleus by uploading the MAX-
698 projection image and the corresponding ROI mask (generated with Cellpose) into Fiji (ImageJ;
699 National Institutes of Health). Mean intensity was calculated for each ROI, and a threshold
700 was applied to distinguish marker-positive cells from background immunostaining. Only cells
701 above this threshold were counted, and the ratio to the total number of nuclei (ROIs in the

702 mask) was determined. Nuclei smaller than 20 µm² were excluded, as they were considered
703 pycnotic cells.
704 For quantitative analyses of ZO1 staining at the apical side of the cells, positive areas were
705 defined and measured by manually setting common thresholds in Fiji for all genotypes. For
706 each image, the DAPI positive area was also determined and measured by manually setting
707 thresholds. The percentage of ZO1 positive area per organoid slice was determined after
708 dividing the ZO1 calculated area by the DAPI area.
709 Analysis of ciliary density was performed by manually counting the number of cilia axonemes
710 (INPP5E staining) over the number of basal bodies (Gamma-Tubulin staining). Measurements
711 of axonemal INPP5E intensity and ciliary length were performed on unprocessed images (raw
712 data) using a custom Matlab script for recognizing and measuring ROIs (cilia) properties. After
713 quantifications were performed, representative images were processed by means of
714 background subtraction and contrast settings via Fiji.
715 All data are presented as mean ± SEM. One-Way ANOVA Kruskal-Wallis and Dunn's test were
716 performed and the following statistical significances were considered: *P<0.033, **P<0.0021,
717 ***P<0.0002 and ****P<0.0001. All statistical data analysis and graph illustrations were
718 performed using GraphPad Prism (GraphPad Software).
719
720 **Total RNA isolation and qPCR analyses**
721 Control, *RPGRIP1L* KO and JBTS patient-derived cerebellar organoids from different hiPSCs
722 lines (Ph2, Wtc11, NG2266) and several independent experiments were collected every seven
723 days from day 7 to 35 of the differentiation protocol and washed with PBS. RNA was isolated
724 using the RNeasy Kit (Qiagen #74104) and RNAse-free DNase Set (Qiagen #79254) following
725 manufacturer's instructions. 1µg of isolated RNA was retro-transcribed into cDNA using the
726 GoScript Reverse Transcriptase Kit (Promega #A5001). For quantitative real-time PCR, a cDNA
727 dilution (equal to 15 ng of starting RNA per well) was used in a Maxima SYBR Green/ROX qPCR
728 Master Mix 2x (Thermo Scientific #K0222). Duplicate reactions for each sample were prepared
729 and the samples were run in a Step One Real-Time PCR System Thermal Cycling Block (Applied
730 Biosystems #4376357). GAPDH housekeeping gene was used as reference. Primer pairs are
731 listed in **Supplementary Table 7.** The analysis of real-time data was performed using the
732 included StepOne Software version 2.0 and graphs were generated using GraphPad Prism
733 (GraphPad Software).

734

735 **Total RNA isolation and Bulk RNAseq analysis on cerebellar organoids**

736 RNA was isolated as described above using the RNeasy Kit (Qiagen #74104) and RNAse-free
737 DNase Set (Qiagen #79254) from control, *RPGRIP1L* KO and JBTS patient-derived cerebellar
738 organoids at different timepoint and from several independent experiments (see
739 Supplementary Tables 2-4 for sample details and N). RNA quality was determined by
740 measuring the RNA integrity number (RIN) via the High Sensitive RNA Screen Tape Analysis kit
741 (Agilent Technologies #5067) on the TapeStation system (Agilent Technologies). A RIN above
742 9.5 was considered as good quality RNA and 250 ng RNA in a total volume of 25 µl was
743 prepared per sample for further procedure. Bulk RNAseq was realized by the Genotyping and
744 Sequencing Core Facility of the Paris Brain Institute (iGenSeq, ICM Paris). Poly A stranded cDNA
745 libraries were built with the kit "Illumina® Stranded mRNA Prep" and their quality checked on
746 "AGILENT Tapestation 2100". 125 ng of each library was sequenced on both strands to produce
747 between 33-44 Millions reads (100 bases long) using a Novaseq6000 ILLUMINA.

748 RNAseq data processing was performed in Galaxy under supervision of the ARTBio platform
749 (IBPS, Paris). Paired-end RNA reads were aligned against the homo sapiens hg38 genome by
750 using the STAR aligner (v2.7.10, Galaxy wrapper v4) [100] and the gene annotations gtf files
751 GRCh38.109. Quality of sequencing was controlled with fastQC (Galaxy wrapper
752 v0.74+galaxy0) and MultiQC (Galaxy wrapper v1.11+galaxy1) [101]. Gene expression was
753 assessed by counting sequencing reads aligned to gene exons with featureCounts (Galaxy
754 wrapper v2.0.3+galaxy2) [102]. Raw counts were further converted to normalized gene
755 expression values using the log2(tpm+1) transformation where tpm is the count of transcript
756 aligned reads per length of transcript (kb) per million of total mapped reads (Galaxy tool
757 "cpm_tpm_rpk" v0.5.2) and heatmap visualizations were produced with the Galaxy tool
758 "high_dim_heatmap" (v3.1.3+galaxy0) using the normalized gene expression values.
759 Differentially expressed genes (DEGs) were selected from the gene raw read counts using
760 DESeq2 (Galaxy wrapper v2.11.40.8+galaxy0) [103] and the Benjamini-Hochberg p-adjusted
761 cutoff 0.05. DESeq2 statistical tables were used for generation of Volcano Plots (Galaxy tool id
762 "volcanoplot" v0.0.5) [104] and for the analysis of overrepresented gene ontology (GO)
763 categories (Metascape online software, https://metascape.org/gp/index.html#/main/step1)
764 [105].

765

ACKNOWLEDGEMENTS

We particularly thank Chloé Chaumeton and France Lam from the IBPS imaging platform I2PS for their help on image acquisition. We thank the IBPS Bioinformatics facility of which C.A. is a former member. We thank the iGenSeq sequencing platform at the ICM for reliable and fast processing of our samples. We are very grateful to Stéphane Nedelec for providing advice on BGJ-398/Infigratinib drug usage in hiPSCs and to Aline Stedman for scientific discussions and advices on manuscript organization. We thank Alexis Eschstruth for his kind contribution to the PCR analysis to identify the cDNA product of JBTS patient c.2304+1G>T splice variant. We are very grateful to Pierre Luc Bardet for his advice in generating custom Matlab scripts for cilia analysis. We thank Virginie Sottile for her support. This work was supported by funding to SSM from the *Fondation pour la Recherche Médicale (“Equipe FRM”* projects EQU201903007943 and EQU202503020010), from the *Fondation pour la Recherche sur le Cancer* (ARCPJA2024080008603), from the *Agence Nationale de la Recherche* - ERA-NET Neuron 2021 “NDCil” (ANR-21-NEU2-0009-03) project and PRC AAPG2024 “CiCerO” project, from the *Fondation Maladies Rares* and the *Association Mieux vivre avec le syndrome de Joubert* under the reference “ASSOJoubert_2024_Schneider”. L.B.’s PhD was funded by Sorbonne Université (Doctoral school *Complexité du Vivant* ED515). A.W. received funding from the German Research Foundation (DFG; WI 5451/1-1). Work in E.M.V.’s lab was supported by Italian Ministry of Health - ERA-NET Neuron 2021 “NDCil” (ERP-2021-23680733).

BIBLIOGRAPHY

1. Stoodley, C. J. The Cerebellum and Neurodevelopmental Disorders. *The Cerebellum* **15**, 34–37 (2016).
2. Leto, K. *et al.* Consensus Paper: Cerebellar Development. *The Cerebellum* **15**, 789–828 (2016).
3. Crossley, P. H., Martinez, S. & Martin, G. R. Midbrain development induced by FGF8 in the chick embryo. *Nature* **380**, 66–68 (1996).
4. Chi, C. L., Martinez, S., Wurst, W. & Martin, G. R. The isthmic organizer signal FGF8 is required for cell survival in the prospective midbrain and cerebellum. *Development* **130**, 2633–2644 (2003).
5. Hoshino, M. *et al.* Ptf1a, a bHLH Transcriptional Gene, Defines GABAergic Neuronal Fates in Cerebellum. *Neuron* **47**, 201–213 (2005).

801 6. Ben-Arie, N. *et al.* Math1 is essential for genesis of cerebellar granule neurons. *Nature*
802 **390**, 169–172 (1997).
803 7. Machold, R. & Fishell, G. Math1 Is Expressed in Temporally Discrete Pools of Cerebellar
804 Rhombic-Lip Neural Progenitors. *Neuron* **48**, 17–24 (2005).
805 8. Rakic, P. & Sidman, R. L. Histogenesis of cortical layers in human cerebellum,
806 particularly the lamina dissecans. *J. Comp. Neurol.* **139**, 473–500 (1970).
807 9. Aldinger, K. A. *et al.* Spatial and cell type transcriptional landscape of human cerebellar
808 development. *Nat. Neurosci.* **24**, 1163–1175 (2021).
809 10. Haldipur, P. *et al.* Spatiotemporal expansion of primary progenitor zones in the
810 developing human cerebellum. *Science* **366**, 454–460 (2019).
811 11. Sillitoe, R. V. & Joyner, A. L. Morphology, Molecular Codes, and Circuitry Produce the
812 Three-Dimensional Complexity of the Cerebellum. *Annu. Rev. Cell Dev. Biol.* **23**, 549–577
813 (2007).
814 12. Maria, B. L. *et al.* 'Joubert Syndrome' Revisited: Key Ocular Motor Signs With Magnetic
815 Resonance Imaging Correlation. *J. Child Neurol.* **12**, 423–430 (1997).
816 13. Bachmann-Gagescu, R. *et al.* Healthcare recommendations for Joubert syndrome. *Am. J.*
817 *Med. Genet. A.* **182**, 229–249 (2020).
818 14. Bachmann-Gagescu, R. *et al.* Joubert syndrome: a model for untangling recessive
819 disorders with extreme genetic heterogeneity. *J. Med. Genet.* **52**, 514–522 (2015).
820 15. Serpieri, V. *et al.* Recurrent, founder and hypomorphic variants contribute to the
821 genetic landscape of Joubert syndrome. *J. Med. Genet.* **60**, 885–893 (2023).
822 16. Mitchison, H. M. & Valente, E. M. Motile and non-motile cilia in human pathology: from
823 function to phenotypes: Motile and non-motile ciliopathies. *J. Pathol.* **241**, 294–309
824 (2017).
825 17. Reiter, J. F. & Leroux, M. R. Genes and molecular pathways underpinning ciliopathies.
826 *Nat. Rev. Mol. Cell Biol.* **18**, 533–547 (2017).
827 18. Mill, P., Christensen, S. T. & Pedersen, L. B. Primary cilia as dynamic and diverse
828 signalling hubs in development and disease. *Nat. Rev. Genet.* **24**, 421–441 (2023).
829 19. Goetz, S. C. & Anderson, K. V. The primary cilium: a signalling centre during vertebrate
830 development. *Nat. Rev. Genet.* **11**, 331–344 (2010).
831 20. Reiter, J. F., Blacque, O. E. & Leroux, M. R. The base of the cilium: roles for transition
832 fibres and the transition zone in ciliary formation, maintenance and
833 compartmentalization. *EMBO Rep.* **13**, 608–618 (2012).
834 21. Jensen, V. L. *et al.* Formation of the transition zone by Mks5/Rpgrip1L establishes a
835 ciliary zone of exclusion (CIZE) that compartmentalises ciliary signalling proteins and
836 controls PIP_2 ciliary abundance. *EMBO J.* **34**, 2537–2556 (2015).
837 22. Wiegering, A. *et al.* Rpgrip1l controls ciliary gating by ensuring the proper amount of
838 Cep290 at the vertebrate transition zone. *Mol. Biol. Cell* **32**, 675–689 (2021).
839 23. Besse, L. *et al.* Primary cilia control telencephalic patterning and morphogenesis via Gli3
840 proteolytic processing. *Development* **138**, 2079–2088 (2011).
841 24. Andreu-Cervera, A. *et al.* The ciliopathy gene *ftm/rpgrip1l* controls mouse forebrain
842 patterning via region-specific modulation of hedgehog/gli signaling. *J. Neurosci.* 2199–
843 18 (2019) doi:10.1523/JNEUROSCI.2199-18.2019.
844 25. Chang, C.-H. *et al.* Atoh1 Controls Primary Cilia Formation to Allow for SHH-Triggered
845 Granule Neuron Progenitor Proliferation. *Dev. Cell* **48**, 184-199.e5 (2019).
846 26. Ong, T., Trivedi, N., Wakefield, R., Frase, S. & Solecki, D. J. Siah2 integrates mitogenic
847 and extracellular matrix signals linking neuronal progenitor ciliogenesis with germinal

zone occupancy. *Nat. Commun.* **11**, 5312 (2020).
27. Ott, C. M. *et al.* Permanent deconstruction of intracellular primary cilia in differentiating granule cell neurons. *J. Cell Biol.* **223**, e202404038 (2024).
28. Chizhikov, V. V. *et al.* Cilia Proteins Control Cerebellar Morphogenesis by Promoting Expansion of the Granule Progenitor Pool. *J. Neurosci.* **27**, 9780–9789 (2007).
29. Spassky, N. *et al.* Primary cilia are required for cerebellar development and Shh-dependent expansion of progenitor pool. *Dev. Biol.* **317**, 246–259 (2008).
30. Delous, M. *et al.* The ciliary gene RPGRIP1L is mutated in cerebello-oculo-renal syndrome (Joubert syndrome type B) and Meckel syndrome. *Nat. Genet.* **39**, 875–881 (2007).
31. Lancaster, M. A. *et al.* Defective Wnt-dependent cerebellar midline fusion in a mouse model of Joubert syndrome. *Nat. Med.* **17**, 726–731 (2011).
32. Abdelhamed, Z. A. *et al.* The ciliary Frizzled-like receptor Tmem67 regulates canonical Wnt/β-catenin signalling in the developing cerebellum via Hoxb5. *Sci. Rep.* **9**, 5446 (2019).
33. Damerla, R. R. *et al.* Novel Jbts17 mutant mouse model of Joubert syndrome with cilia transition zone defects and cerebellar and other ciliopathy related anomalies. *Hum. Mol. Genet.* **24**, 3994–4005 (2015).
34. Bashford, A. L. & Subramanian, V. Mice with a conditional deletion of *Talpid3* (*KIAA0586*) – a model for Joubert syndrome. *J. Pathol.* **248**, 396–408 (2019).
35. Suciu, S. K., Long, A. B. & Caspary, T. Smoothened and ARL13B are critical in mouse for superior cerebellar peduncle targeting. *Genetics* **218**, iyab084 (2021).
36. Aguilar, A. *et al.* Analysis of human samples reveals impaired SHH-dependent cerebellar development in Joubert syndrome/Meckel syndrome. *Proc. Natl. Acad. Sci.* **109**, 16951–16956 (2012).
37. Muguruma, K., Nishiyama, A., Kawakami, H., Hashimoto, K. & Sasai, Y. Self-Organization of Polarized Cerebellar Tissue in 3D Culture of Human Pluripotent Stem Cells. *Cell Rep.* **10**, 537–550 (2015).
38. Nayler, S. P. & Becker, E. B. E. The Use of Stem Cell-Derived Neurons for Understanding Development and Disease of the Cerebellum. *Front. Neurosci.* **Volume 12-2018**, (2018).
39. Silva, T. P. *et al.* Maturation of Human Pluripotent Stem Cell-Derived Cerebellar Neurons in the Absence of Co-culture. *Front. Bioeng. Biotechnol.* **8**, 70 (2020).
40. Atamian, A. *et al.* Human cerebellar organoids with functional Purkinje cells. *Cell Stem Cell* **31**, 39-51.e6 (2024).
41. Kagermeier, T. *et al.* Human organoid model of pontocerebellar hypoplasia 2a recapitulates brain region-specific size differences. (2024).
42. Guerra, M., Medici, V., La Sala, G. & Farini, D. Unravelling the Cerebellar Involvement in Autism Spectrum Disorders: Insights into Genetic Mechanisms and Developmental Pathways. *Cells* **13**, (2024).
43. Ryu, S. *et al.* Modeling Friedreich's ataxia with Bergmann glia-enriched human cerebellar organoids. *bioRxiv* 2025.05.16.654315 (2025) doi:10.1101/2025.05.16.654315.
44. Aprile, D. *et al.* Benchmarking cerebellar organoids to model autism spectrum disorder and human brain evolution. *bioRxiv* 2025.05.14.653684 (2025) doi:10.1101/2025.05.14.653684.
45. Wiegering, A. *et al.* A differential requirement for ciliary transition zone proteins in human and mouse neural progenitor fate specification. *Nat. Commun.* **16**, 3258 (2025).

895 46. Andreu-Cervera, A., Catala, M. & Schneider-Maunoury, S. Cilia, ciliopathies and
896 hedgehog-related forebrain developmental disorders. *Neurobiol. Dis.* **150**, 105236
897 (2021).
898 47. Silva, T. P. *et al.* Transcriptome profiling of human pluripotent stem cell-derived
899 cerebellar organoids reveals faster commitment under dynamic conditions. *Biotechnol.*
900 *Bioeng.* **118**, 2781–2803 (2021).
901 48. Li, M. *et al.* Integrative functional genomic analysis of human brain development and
902 neuropsychiatric risks. *Science* **362**, eaat7615 (2018).
903 49. Wechsler-Reya, R. J. & Scott, M. P. Control of Neuronal Precursor Proliferation in the
904 Cerebellum by Sonic Hedgehog. *Neuron* **22**, 103–114 (1999).
905 50. Pollara, L. *et al.* Production and characterisation of four Joubert syndrome patient-
906 derived induced pluripotent stem cell (iPSC) lines with mutations in either RPGRIP1L or
907 CPLANE1 genes. *Stem Cell Res.* **86**, 103734 (2025).
908 51. Richards, S. *et al.* Standards and guidelines for the interpretation of sequence variants:
909 a joint consensus recommendation of the American College of Medical Genetics and
910 Genomics and the Association for Molecular Pathology. *Genet. Med.* **17**, 405–424
911 (2015).
912 52. Wiegering, A. *et al.* Cell type-specific regulation of ciliary transition zone assembly in
913 vertebrates. *EMBO J.* **37**, (2018).
914 53. Taverna, E. & Huttner, W. B. Neural Progenitor Nuclei IN Motion. *Neuron* **67**, 906–914
915 (2010).
916 54. Das, R. M. & Storey, K. G. Apical Abscission Alters Cell Polarity and Dismantles the
917 Primary Cilium During Neurogenesis. *Science* **343**, 200–204 (2014).
918 55. Laguesse, S., Peyre, E. & Nguyen, L. Progenitor genealogy in the developing cerebral
919 cortex. *Cell Tissue Res.* **359**, 17–32 (2015).
920 56. Sokpor, G., Brand-Saberi, B., Nguyen, H. P. & Tuoc, T. Regulation of Cell Delamination
921 During Cortical Neurodevelopment and Implication for Brain Disorders. *Front. Neurosci.*
922 **16**, 824802 (2022).
923 57. Gratton, M.-O. *et al.* Hes6 Promotes Cortical Neurogenesis and Inhibits Hes1
924 Transcription Repression Activity by Multiple Mechanisms. *Mol. Cell. Biol.* **23**, 6922–
925 6935 (2003).
926 58. Murai, K., Philpott, A. & Jones, P. H. Hes6 Is Required for the Neurogenic Activity of
927 Neurogenin and NeuroD. *PLoS ONE* **6**, e27880 (2011).
928 59. Behesti, H., Kocabas, A., Buchholz, D. E., Carroll, T. S. & Hatten, M. E. Altered temporal
929 sequence of transcriptional regulators in the generation of human cerebellar granule
930 cells. *eLife* **10**, e67074 (2021).
931 60. Arellano, J. I., Guadiana, S. M., Breunig, J. J., Rakic, P. & Sarkisian, M. R. Development
932 and distribution of neuronal cilia in mouse neocortex. *J. Comp. Neurol.* **520**, 848–873
933 (2012).
934 61. Wu, J. Y. *et al.* Mapping of neuronal and glial primary cilia contactome and connectome
935 in the human cerebral cortex. *Neuron* **112**, 41-55.e3 (2024).
936 62. Jenks, A. D. *et al.* Primary Cilia Mediate Diverse Kinase Inhibitor Resistance Mechanisms
937 in Cancer. *Cell Rep.* **23**, 3042–3055 (2018).
938 63. Nita, A. *et al.* FGFR2 residence in primary cilia is necessary for epithelial cell signaling. *J.*
939 *Cell Biol.* **224**, e202311030 (2025).
940 64. Long, K. R. & Huttner, W. B. How the extracellular matrix shapes neural development.
941 *Open Biol.* **9**, 180216 (2019).

942 65. Álvarez, Z. *et al.* Artificial extracellular matrix scaffolds of mobile molecules enhance
943 maturation of human stem cell-derived neurons. *Cell Stem Cell* **30**, 219-238.e14 (2023).
944 66. Yang, L., Wei, M., Xing, B. & Zhang, C. Extracellular matrix and synapse formation.
945 *Biosci. Rep.* **43**, BSR20212411 (2023).
946 67. Joyner, A. L., Liu, A. & Millet, S. Otx2, Gbx2 and Fgf8 interact to position and maintain a
947 mid–hindbrain organizer. *Curr. Opin. Cell Biol.* **12**, 736–741 (2000).
948 68. Sato, T. & Joyner, A. L. The duration of *Fgf8* isthmic organizer expression is key to
949 patterning different tectal-isthmo-cerebellum structures. *Development* **136**, 3617–3626
950 (2009).
951 69. Green, M. J. *et al.* Independently specified *Atoh1* domains define novel developmental
952 compartments in rhombomere 1. *Development* **141**, 389–398 (2014).
953 70. Suzuki-Hirano, A., Harada, H., Sato, T. & Nakamura, H. Activation of Ras-ERK pathway by
954 Fgf8 and its downregulation by Sprouty2 for the isthmus organizing activity. *Dev. Biol.*
955 **337**, 284–293 (2010).
956 71. Yu, T., Yaguchi, Y., Echevarria, D., Martinez, S. & Basson, M. A. Sprouty genes prevent
957 excessive FGF signalling in multiple cell types throughout development of the
958 cerebellum. *Development* **138**, 2957–2968 (2011).
959 72. Del Corral, R. D., Breitkreuz, D. N. & Storey, K. G. Onset of neuronal differentiation is
960 regulated by paraxial mesoderm and requires attenuation of FGF signalling.
961 *Development* **129**, 1681–1691 (2002).
962 73. Wilcock, A. C., Swedlow, J. R. & Storey, K. G. Mitotic spindle orientation distinguishes
963 stem cell and terminal modes of neuron production in the early spinal cord.
964 *Development* **134**, 1943–1954 (2007).
965 74. Olivera-Martinez, I. & Storey, K. G. Wnt signals provide a timing mechanism for the FGF-
966 retinoid differentiation switch during vertebrate body axis extension. *Development* **134**,
967 2125–2135 (2007).
968 75. Lukaszewicz, A., Savatier, P., Cortay, V., Kennedy, H. & Dehay, C. Contrasting Effects of
969 Basic Fibroblast Growth Factor and Neurotrophin 3 on Cell Cycle Kinetics of Mouse
970 Cortical Stem Cells. *J. Neurosci.* **22**, 6610–6622 (2002).
971 76. Gantner, C. W. *et al.* FGF-MAPK signaling regulates human deep-layer corticogenesis.
972 *Stem Cell Rep.* **16**, 1262–1275 (2021).
973 77. Basson, M. A. *et al.* Specific regions within the embryonic midbrain and cerebellum
974 require different levels of FGF signaling during development. *Development* **136**, 1962–
975 1962 (2009).
976 78. Catala, M. Development of the Central Nervous System. in *Textbook of Pediatric*
977 *Neurosurgery* (eds. Di Rocco, C., Pang, D. & Rutka, J. T.) 1–99 (Springer International
978 Publishing, Cham, 2019). doi:10.1007/978-3-319-31512-6_1-1.
979 79. Watson, C., Shimogori, T. & Puelles, L. Mouse *Fgf8* -Cre-LacZ lineage analysis defines the
980 territory of the postnatal mammalian isthmus. *J. Comp. Neurol.* **525**, 2782–2799 (2017).
981 80. Kasberg, A. D., Brunskill, E. W. & Steven Potter, S. SP8 regulates signaling centers during
982 craniofacial development. *Dev. Biol.* **381**, 312–323 (2013).
983 81. Wagner, A. E. *et al.* SP8 Promotes an Aggressive Phenotype in Hepatoblastoma via FGF8
984 Activation. *Cancers* **12**, (2020).
985 82. Sahara, S., Kawakami, Y., Izpisua Belmonte, J. C. & O'Leary, D. D. Sp8 exhibits reciprocal
986 induction with Fgf8 but has an opposing effect on anterior-posterior cortical area
987 patterning. *Neural Develop.* **2**, 10 (2007).
988 83. Hämmerle, B. *et al.* Transient expression of Mnb/Dyrk1a couples cell cycle exit and

989 differentiation of neuronal precursors by inducing p27KIP1 expression and suppressing
990 NOTCH signaling. *Development* **138**, 2543–2554 (2011).
991 84. Sudarov, A. *et al.* Ascl1 Genetics Reveals Insights into Cerebellum Local
992 Circuit Assembly. *J. Neurosci.* **31**, 11055 (2011).
993 85. Cerrato, V. *et al.* Multiple origins and modularity in the spatiotemporal emergence of
994 cerebellar astrocyte heterogeneity. *PLOS Biol.* **16**, e2005513 (2018).
995 86. Louvi, A., Alexandre, P., Métin, C., Wurst, W. & Wassef, M. The isthmic neuroepithelium
996 is essential for cerebellar midline fusion. *Development* **130**, 5319–5330 (2003).
997 87. Waas, B. *et al.* Dual and opposing roles for the kinesin-2 motor, KIF17, in Hedgehog-
998 dependent cerebellar development. *Sci. Adv.* **10**, eade1650.
999 88. Jiwani, T., Kim, J. J. & Rosenblum, N. D. Suppressor of Fused (Sufu) controls cerebellum
1000 granule cell proliferation by suppressing Fgf8 and spatially regulating Gli proteins.
1001 *Development* dev.170274 (2020) doi:10.1242/dev.170274.
1002 89. Kim, J. J. *et al.* Suppressor of Fused Controls Mid-Hindbrain Patterning and Cerebellar
1003 Morphogenesis via GLI3 Repressor. *J. Neurosci.* **31**, 1825–1836 (2011).
1004 90. Yabut, O. R. *et al.* Aberrant FGF signaling promotes granule neuron precursor expansion
1005 in SHH subgroup infantile medulloblastoma. https://doi.org/10.7554/elife.100767.2
1006 (2024) doi:10.7554/elife.100767.2.
1007 91. De Mori, R. *et al.* Hypomorphic Recessive Variants in SUFU Impair the Sonic Hedgehog
1008 Pathway and Cause Joubert Syndrome with Cranio-facial and Skeletal Defects. *Am. J.*
1009 *Hum. Genet.* **101**, 552–563 (2017).
1010 92. Serpieri, V. *et al.* SUFU haploinsufficiency causes a recognisable
1011 neurodevelopmental phenotype at the mild end of the Joubert syndrome spectrum. *J.*
1012 *Med. Genet.* **59**, 888 (2022).
1013 93. Brugières, L. *et al.* High Frequency of Germline SUFU Mutations in Children With
1014 Desmoplastic/Nodular Medulloblastoma Younger Than 3 Years of Age. *J. Clin. Oncol.* **30**,
1015 2087–2093 (2012).
1016 94. Guerrini-Rousseau, L. *et al.* Germline SUFU mutation carriers and medulloblastoma:
1017 clinical characteristics, cancer risk, and prognosis. *Neuro-Oncol.* **20**, 1122–1132 (2018).
1018 95. Roepman, R. *et al.* Interaction of nephrocystin-4 and RPGRIP1 is disrupted by
1019 nephronophthisis or Leber congenital amaurosis-associated mutations. *Proc. Natl. Acad.*
1020 *Sci.* **102**, 18520–18525 (2005).
1021 96. Arts, H. H. *et al.* Mutations in the gene encoding the basal body protein RPGRIP1L, a
1022 nephrocystin-4 interactor, cause Joubert syndrome. *Nat. Genet.* **39**, 882–888 (2007).
1023 97. Sang, L. *et al.* Mapping the NPHP-JBTS-MKS Protein Network Reveals Ciliopathy Disease
1024 Genes and Pathways. *Cell* **145**, 513–528 (2011).
1025 98. Demuynck, B. *et al.* Infigratinib low dose therapy is an effective strategy to treat
1026 hypochondroplasia. *J. Bone Miner. Res.* zjaf088 (2025) doi:10.1093/jbmr/zjaf088.
1027 99. Poretti, A. *et al.* Joubert syndrome: neuroimaging findings in 110 patients in correlation
1028 with cognitive function and genetic cause. *J. Med. Genet.* **54**, 521 (2017).
1029 100. Dobin, A. *et al.* STAR: ultrafast universal RNA-seq aligner. *Bioinformatics* **29**, 15–21
1030 (2013).
1031 101. Ewels, P., Magnusson, M., Lundin, S. & Käller, M. MultiQC: summarize analysis results
1032 for multiple tools and samples in a single report. *Bioinformatics* **32**, 3047–3048 (2016).
1033 102. Liao, Y., Smyth, G. K. & Shi, W. featureCounts: an efficient general purpose program for
1034 assigning sequence reads to genomic features. *Bioinformatics* **30**, 923–930 (2014).
1035 103. Love, M. I., Huber, W. & Anders, S. Moderated estimation of fold change and dispersion

1036 for RNA-seq data with DESeq2. *Genome Biol.* **15**, 550 (2014).
1037 104. Zink, R. C., Wolfinger, R. D. & Mann, G. Summarizing the incidence of adverse events
1038 using volcano plots and time intervals. *Clin. Trials* **10**, 398–406 (2013).
1039 105. Zhou, Y. *et al.* Metascape provides a biologist-oriented resource for the analysis of
1040 systems-level datasets. *Nat. Commun.* **10**, 1523 (2019).
1041

1042 **FIGURE 1. *RPGRIP1L*-deficient cerebellar organoids present a severe reduction of Purkinje**
1043 **cell markers and a mild decrease of glutamatergic lineage markers**
1044 **(A)** Diagram of the 3D cerebellar differentiation protocol. Time-line and drugs (SB: SMAD
1045 antagonists SB-431542; FGF2: Fibroblast growth factor 2; FGF19: Fibroblast growth factor 19;
1046 SDF1: stromal cell-derived factor 1) are indicated on top, culture media at the bottom. The
1047 blue circular arrow on top indicates orbital rotation. Protocol modified after [39] **(B)** Schematic
1048 representation of the RPGRIP1L protein and relative position of the mutations present in
1049 hiPSC lines. In both *RPGRIP1L* KO lines (Ph2 in purple, Wtc11 in pink) homozygous frameshift
1050 mutations result in premature stop codon before the first coiled-coil (CC) domain. JBTS
1051 patient (NG2266 in green) variants p.Q684X and c.2304+1G>T result in stop codons between
1052 the first and the second C2 domain. **(C)** Brain marker gene expression in cerebellar organoids
1053 at day 7. Heatmap based on the normalized expression values of selected brain marker genes.
1054 Z score was calculated on the log2(tpm+1) data from the bulk RNASeq analysis. Right: scheme
1055 of the gene expression domains in the E9.5 mouse brain. MHB: midbrain-hindbrain boundary.
1056 Thinner box for Wnt1: expression restricted to the roof plate. See supplementary Table 1 for
1057 number of independent experimental replicates (N) and sample numbering. **(D, E)** Graphs
1058 showing temporal gene expression analysis of Purkinje cells (*OLIG2* and *CALB1*) (D) and
1059 glutamatergic (*BARHL1* and *ATOH1*) (E) lineage markers in control (blue), *RPGRIP1L* KO
1060 (magenta), and JBTS patient-derived (green) organoids throughout differentiation.
1061 Normalized gene expression (Log2(tpm+1)) values from bulk RNASeq analysis are displayed
1062 as mean ± SEM. More than 20 organoids were analyzed per condition per experiment. For
1063 control and *RPGRIP1L* KO, data were obtained from both Ph2 and Wtc11 lines. Day 0 (hiPSCs):
1064 N=2 for controls, N=2 for RPGRIP1L KO, N=1 for JBTS patient line; day 7-35 organoids: see
1065 Supplementary Table 2 for number of independent experimental replicates. **(F)**
1066 Immunofluorescence for OLIG2 (Purkinje progenitors) on cryosections from control,
1067 *RPGRIP1L* KO and JBTS patient organoids at day 21. **(G)** Graph showing the % of OLIG2+ over
1068 DAPI+ nuclei. Each dot represents an organoid section. Several sections from different
1069 organoids were analyzed per condition (control: Ph2 N=1, *RPGRIP1L* KO: Ph2 N=1; JBTS
1070 patient: NG2266 N=1). Data are shown as mean ± SEM. Asterisks denote statistical
1071 significance according to One-Way ANOVA Kruskal-Wallis test with Dunn's correction
1072 (***P<0.0002 and ****P< 0.0001). **(H)** Immunofluorescence for CALB1 on cryosections from
1073 day 28 control, *RPGRIP1L* KO and JBTS patient organoids. **(I)** Quantification of the % of CALB1+

1074 cells over DAPI+ nuclei, on > 15 sections from different organoids per experiment per
1075 condition (control and *RPGRIP1L* KO: Ph2 line N=2 – round dots; JBTS patient: NG2266 line
1076 N=2 – squared dots). Data are shown as mean ± SEM. Asterisks denote statistical significance
1077 according to One-Way ANOVA Kruskal-Wallis test with Dunn's correction (****P<0.0001). **(J)**
1078 Immunofluorescence for BARHL1 on cryosections from day 28 control, *RPGRIP1L* KO and JBTS
1079 patient organoids. **(K)** Quantification of the % of BARHL1+ over DAPI+ nuclei, in > 15 sections
1080 from different organoids per experiment per condition (control and *RPGRIP1L* KO: Ph2 line
1081 N=2 – round dots, Wtc11 line N=1 – triangular dots; JBTS patient: NG2266 line N=2 – squared
1082 dots). Data are shown as mean ± SEM. Asterisks denote statistical significance according to
1083 One-Way ANOVA Kruskal-Wallis test with Dunn's correction (****P<0.0001). N: number of
1084 independent experimental replicates. Scale bars: 100 µm in F, H and J.
1085
1086 **FIGURE 2. Organoid size and area of SOX2$^+$/ZO1$^+$ progenitors are increased in *RPGRIP1L*-**
1087 **deficient cerebellar organoids.**
1088 **(A**) Representative bright field images of cerebellar organoids at the indicated time points.
1089 **(B)** Graph representing the organoid growth rate, measured every 7 days from day 7 to day
1090 35. Data are shown as the mean ± SEM of average organoid area from several independent
1091 experiment (N=3 Ph2 line, N=3 Wtc11 line, N=3 NG2266 line, n=10-60 organoids analyzed per
1092 experiment per condition). For control and *RPGRIP1L* KO conditions, data from Ph2 and Wtc11
1093 lines were pooled. Asterisks denote statistical significance according to Two-Way ANOVA test
1094 (*P<0.033, ***P<0.0002, ****P<0.0001). **(C)** Immunofluorescence for SOX2 neural
1095 progenitor marker (magenta) and ZO1 apical marker (green) on cryosections from control,
1096 *RPGRIP1L* KO and JBTS patient organoids at day 14. Examples of small neural rosettes are
1097 circled by dotted lines. **(D)** Quantification of the ZO1+ area over the DAPI+ area in sections
1098 from control, *RPGRIP1L* KO and JBTS patient organoids at day 14. Each dot represents an
1099 organoid section. Several sections from different organoids were analyzed per condition:
1100 control and *RPGRIP1L* KO: N=2 (Ph2 N=1 – round dots, Wtc11 N=1 – triangular dots), JBTS
1101 patient: NG2266 N=1 – squared dots). Mean ± SEM are indicated. Asterisks: statistical
1102 significance according to One-Way ANOVA Kruskal-Wallis test with Dunn's correction (****P<
1103 0.0001) **(E)** Graph showing the % of SOX2$^+$ cells in sections from control, *RPGRIP1L* KO and
1104 JBTS patient organoids at day 14. Each dot represents an organoid section. Several sections
1105 from different organoids were analyzed per condition: control and *RPGRIP1L* KO: N=3 (Ph2

1106 N=1 – round dots, Wtc11 N=2 – triangular dots), JBTS patient: NG2266 N=1 – squared dots).
1107 Mean ± SEM are indicated. Asterisks denote statistical significance according to One-Way
1108 ANOVA Kruskal-Wallis test with Dunn's correction (****P< 0.0001). N: number of
1109 independent experimental replicates. Scale bars: 500 µm in A and 100 µm in C.
1110
1111 **FIGURE 3. Differential requirement of RPGRIP1L protein for ciliogenesis in apical and non-**
1112 **polarized neural progenitors.**
1113 **(A-C)** Immunofluorescence for INPP5E (green) and gamma-TUBULIN (magenta) on sections
1114 from control (A), *RPGRIP1L* KO (B) and JBTS patient (C) organoids at day 14. Scale bar, 10 µm.
1115 The schematic on the left represents the position of the scanned regions: i.e. internal lumen
1116 of neural rosettes. **(D)** Graph showing the quantification of ciliary length. Measures for
1117 individual cilia are represented and the mean value is indicated. Asterisks: statistical
1118 significance according to One-Way ANOVA Kruskal-Wallis and Dunn's test (**P < 0.0021)**. (E-**
1119 **G)** Immunofluorescence for INPP5E (green) and gamma-TUBULIN (magenta) on sections from
1120 control (E), *RPGRIP1L* KO (F) and JBTS patient (G) organoids at day 14. Scale bar, 10 µm. The
1121 schematic on the left represents the position of the scanned regions: i.e. non-polarized tissue.
1122 **(H-J)** Graphs showing quantifications of ciliary properties in non-polarized areas of control,
1123 *RPGRIP1L* KO and JBTS patient cerebellar organoids. Asterisks denote statistical significance
1124 according to One-Way ANOVA Kruskal-Wallis and Dunn's test (**P < 0.0021, ****P < 0.0001).
1125 In **(H)** Ciliary density is calculated as the number of INPP5E+ axonemes over the total number
1126 of gamma-TUBULIN basal bodies per field. Each dot on the graph represents one quantified
1127 field representative for one organoid section. Data are from >15 organoids from independent
1128 experiments and hiPSC lines. Control and *RPGRIP1L* KO: N=2 (Ph2 N=1, Wtc11 N=1); JBTS
1129 patient: NG2266 N=1. In **(I-J)** each dot represents one individual cilium. Average axonemal
1130 INPP5E intensity after background subtraction (I) and average cilia length (J) are calculated
1131 from >200 cilia measured in >15 organoids from independent experiments and hiPSC lines.
1132 Control and *RPGRIP1L* KO: N=2 (Ph2 N=1, Wtc11 N=1); JBTS patient: NG2266 N=1. N: number
1133 of independent experimental replicates. Scale bars: 10 µm in A-C and E-G.
1134
1135 **FIGURE 4. Transcriptome analysis reveals early FGF signaling upregulation and neurogenesis**
1136 **impairment in *RPGRIP1L*-deficient cerebellar organoids**

1137 **(A, B)** Volcano plots representing differentially expressed genes (DEGs) resulting from DESeq2
1138 analysis (only genes with P<0.05; $|\log_2 FC|>1$ are colored) in *RPGRIP1L* KO versus control
1139 condition (A) or in JBTS patient versus control condition (B) at day 14. Selected genes from
1140 representative pathways and cellular processes are circled with different colors as indicated
1141 in the legend on the top right of the panel. **(C)** qPCR analysis of *FGF8* expression levels on
1142 cerebellar organoids at different timepoints (control and *RPGRIP1L* KO: N=6 (Ph2 N=2, Wtc11
1143 N=4); JBTS patient: N=2). Data are shown as individual values; mean ± SEM are indicated.
1144 Asterisks denote statistical significance according to ordinary Two-Way ANOVA performed on
1145 control and *RPGRIP1L* KO samples (*P<0.033, ****P < 0.0001). **(D)** Heatmap representing
1146 normalized RNA expression values of selected DEGs in control and *RPGRIP1L*-deficient
1147 cerebellar organoids over time. 20 organoids were analyzed per condition; See
1148 supplementary Table 2 for number of independent experiments and sample numbering. N:
1149 number of independent experimental replicates.
1150
1151 **FIGURE 5. *RPGRIP1L*-deficient organoids display severe neuronal maturation and**
1152 **extracellular matrix defects as shown by transcriptome analysis**
1153 **(A-B)** Volcano plots representing DEGs resulting from DESeq2 analysis (only genes with
1154 P<0.001, $|\log_2 FC|>2$ are colored) in *RPGRIP1L* KO versus control condition (A) or in JBTS
1155 patient versus control condition (B) at day 28. Selected genes involved in neuronal
1156 differentiation or in building ECM are circled with different colors as indicated in the legend
1157 on the top right of the panel. **(C)** Heatmap representing the normalized RNA expression values
1158 of selected differentially expressed genes in control and *RPGRIP1L*-deficient cerebellar
1159 organoids over time. 20 organoids were analyzed per condition. See supplementary Table 2
1160 for number of independent experiments and sample numbering. **(D-E)** Selected GO-terms
1161 overrepresented among *RPGRIP1L* KO (D) and JBTS patient (E) downregulated genes
1162 extracted from bulk RNA seq DESeq2 lists at day 28. N: number of independent experimental
1163 replicates.
1164
1165 **FIGURE 6. Blocking FGF signaling with BGJ-398 drug rescues neurogenesis in *RPGRIP1L*-**
1166 **deficient cerebellar organoids.**
1167 **(A)** Heatmap representing the normalized RNA expression values over time of selected DEGs
1168 in control and *RPGRIP1L* KO cerebellar organoids, untreated or treated with BGJ-398. See

1169 supplementary Table 3 for sample numbering and number of independent experiments. At
1170 least 20 organoids were analyzed per condition per experiment. **(B)** Heatmap representing
1171 the normalized RNA expression values over time of selected DEGs in JBTS patient-derived
1172 organoids, untreated or treated with BGJ-398. See supplementary Table 4 for sample
1173 numbering and number of independent experiments. At least 20 organoids were analyzed
1174 per condition per experiment. **(C)** Immunofluorescence for SOX2 (gray), NEUROD1 (green)
1175 and HUC/D (magenta) on organoid cryosections from control and *RPGRIP1L*-deficient
1176 untreated or treated with BGJ-398 at day 14. Scale bar, 100 µm. **(D-F)** Graphs showing the %
1177 of NEUROD1+ (D), HUC/D+ (E) and SOX2+ (F) cells over DAPI+ nuclei., counted in > 15 sections
1178 from different organoids per condition per experiment. Controls and *RPGRIP1L* KO: N=3 (Ph2
1179 N=1 – circular dots, Wtc11 N=2 – triangular dots), JBTS: NG2266 N=1 squared dots. Each dot
1180 in the graph represents one organoid; mean ± SEM are shown. Asterisks denote statistical
1181 significance according to One-Way ANOVA Kruskal-Wallis test with Dunn's correction
1182 (**P<0.0021; ****P<0.0001). **(G)** Immunofluorescence for OLIG2 (green) on organoid
1183 cryosections from day 21 control and *RPGRIP1L*-deficient untreated or treated with BGJ-398.
1184 Scale bar, 100 µm. **(H)** Graph showing the % of OLIG2+ over DAPI+ nuclei, counted in several
1185 sections from different organoids per condition. Controls and *RPGRIP1L* KO: N=1 (Ph2 N=1);
1186 JBTS: NG2266 N=1. Each dot in the graph represents one organoid; mean ± SEM are shown.
1187 Asterisks denote statistical significance according to One-Way ANOVA Kruskal-Wallis test with
1188 Dunn's correction (**P<0.0021; ***P<0.0002). N: number of independent experimental
1189 replicates.
1190
1191 **FIGURE 7. EdU pulse-chase experiment shows that neural progenitor proliferation is**
1192 **increased in *RPGRIP1L*-deficient organoids and can be rescued by blocking FGF signaling**
1193 **(A)** Immunofluorescence for SOX2 (magenta) and EdU (green) on organoid cryosections at
1194 day 18 – 2h after EdU pulse, from control and *RPGRIP1L*-deficient (KO and JBTS patient),
1195 untreated or treated with BGJ-398. **(B, C)** Graphs showing the % of EdU+ cells over the DAPI+
1196 nuclei (B) and the % of EdU+/SOX2+ cells over the total number of SOX2+ cells (C) at day 18 –
1197 2h after EdU pulse, counted in several sections from different organoids per condition.
1198 Control and *RPGRIP1L* KO: N=1 (Wtc11); JBTS: N=1 (NG2266). Each dot in the graph represents
1199 one organoid; mean ± SEM are shown. Asterisks: statistical significance according to Ordinary-
1200 Way ANOVA after normal distribution testing (*P<0.033; ****P<0.0001) (B-C). **(D)**

1201 Immunofluorescence for SOX2 (magenta), HUC/D (blue) and EdU (green) on organoid
1202 cryosections at day 23 – 5 days after the 2h EdU pulse (chase experiment), from control and
1203 *RPGRIP1L*-deficient (KO and JBTS patient) untreated or treated with BGJ-398. **(E, F)** Graphs
1204 showing the % of EdU+ cells over the DAPI+ nuclei (E) and the % of EdU+/SOX2+ cells over the
1205 total number of SOX2+ cells at day 23 (chase experiment). Cells were counted in several
1206 sections from different organoids per condition. Control and *RPGRIP1L* KO: N=1 (Wtc11); JBTS:
1207 N=1 (NG2266). Each dot in the graph represents one organoid; mean ± SEM are shown.
1208 Asterisks: statistical significance according to Ordinary-Way ANOVA after normal distribution
1209 testing (**P<0.0021; ****P<0.0001) **(G)** Graph showing the ratio between "strong" and
1210 "faint" EdU labeling in the % of EdU+ cells over total nuclei. Mean ± SEM are shown. N:
1211 number of independent experimental replicates. Scale bars: 100 µm in A and D.
1212
1213
1214
1215
1216
1217
1218
1219
1220
1221
1222
1223
1224
1225
1226
1227
1228
1229
1230
1231

Figure 1

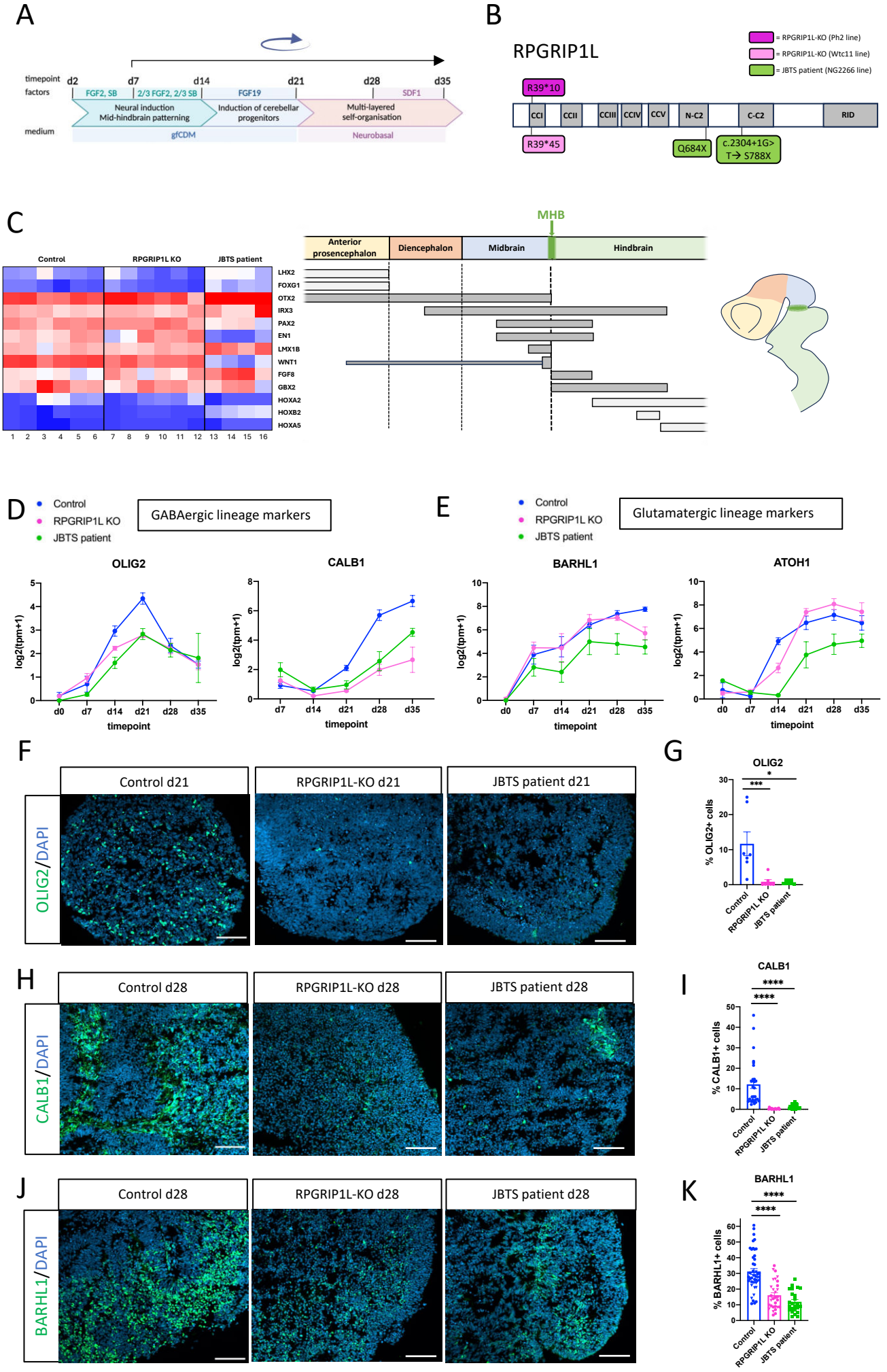
A
timepoint
factors
medium
d2
d7
d14
d21
d28
d35
FGF2, SB
2/3 FGF2, 2/3 SB
FGF19
SDF1
Neural induction
Mid-hindbrain patterning
Induction of cerebellar
progenitors
Multi-layered
self-organisation
gfCDM
Neurobasal
B
RPGRIP1L
= RPGRIP1L-KO (Ph2 line)
= RPGRIP1L-KO (Wtc11 line)
= JBTS patient (NG2266 line)
R39*10
CCI
CCII
CCIII
CCIV
CCV
N-C2
C-C2
RID
R39*45
Q684X
c.2304+1G>
T→ S788X
C
Control
RPGRIP1L KO
JBTS patient
MHB
Anterior
prosencephalon
Diencephalon
Midbrain
Hindbrain
LHX2
FOXG1
OTX2
IRX3
PAX2
EN1
LMX1B
WNT1
FGF8
GBX2
HOXA2
HOXB2
HOXA5
D
Control
RPGRIP1L KO
JBTS patient
GABAergic lineage markers
OLIG2
CALB1
log2(tpm+1)
timepoint
E
Glutamatergic lineage markers
BARHL1
ATOH1
F
Control d21
RPGRIP1L-KO d21
JBTS patient d21
OLIG2/DAPI
G
OLIG2
% OLIG2+ cells
H
Control d28
RPGRIP1L-KO d28
JBTS patient d28
CALB1/DAPI
I
CALB1
% CALB1+ cells
J
Control d28
RPGRIP1L-KO d28
JBTS patient d28
BARHL1/DAPI
K
BARHL1
% BARHL1+ cells

Figure 2

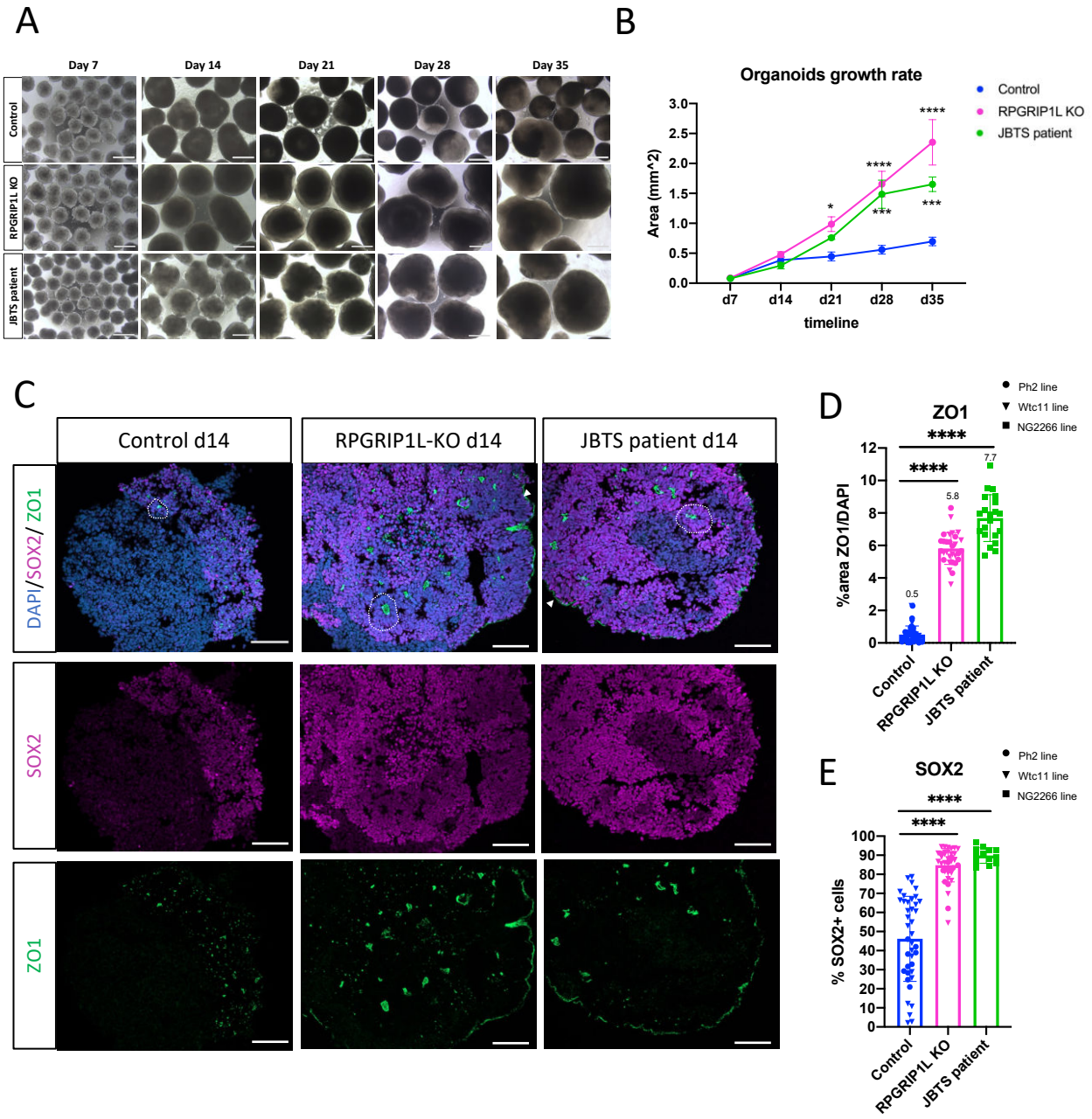
A
Day 7
Day 14
Day 21
Day 28
Day 35
Control
RPGRIP1L KO
JBTS patient
B
Organoids growth rate
Area (mm^2)
timeline
d7
d14
d21
d28
d35
Control
RPGRIP1L KO
JBTS patient
C
Control d14
RPGRIP1L-KO d14
JBTS patient d14
DAPI/SOX2/ ZO1
SOX2
ZO1
D
ZO1
%area ZO1/DAPI
Ph2 line
Wtc11 line
NG2266 line
Control
RPGRIP1L KO
JBTS patient
E
SOX2
% SOX2+ cells
Ph2 line
Wtc11 line
NG2266 line
Control
RPGRIP1L KO
JBTS patient

Figure 3

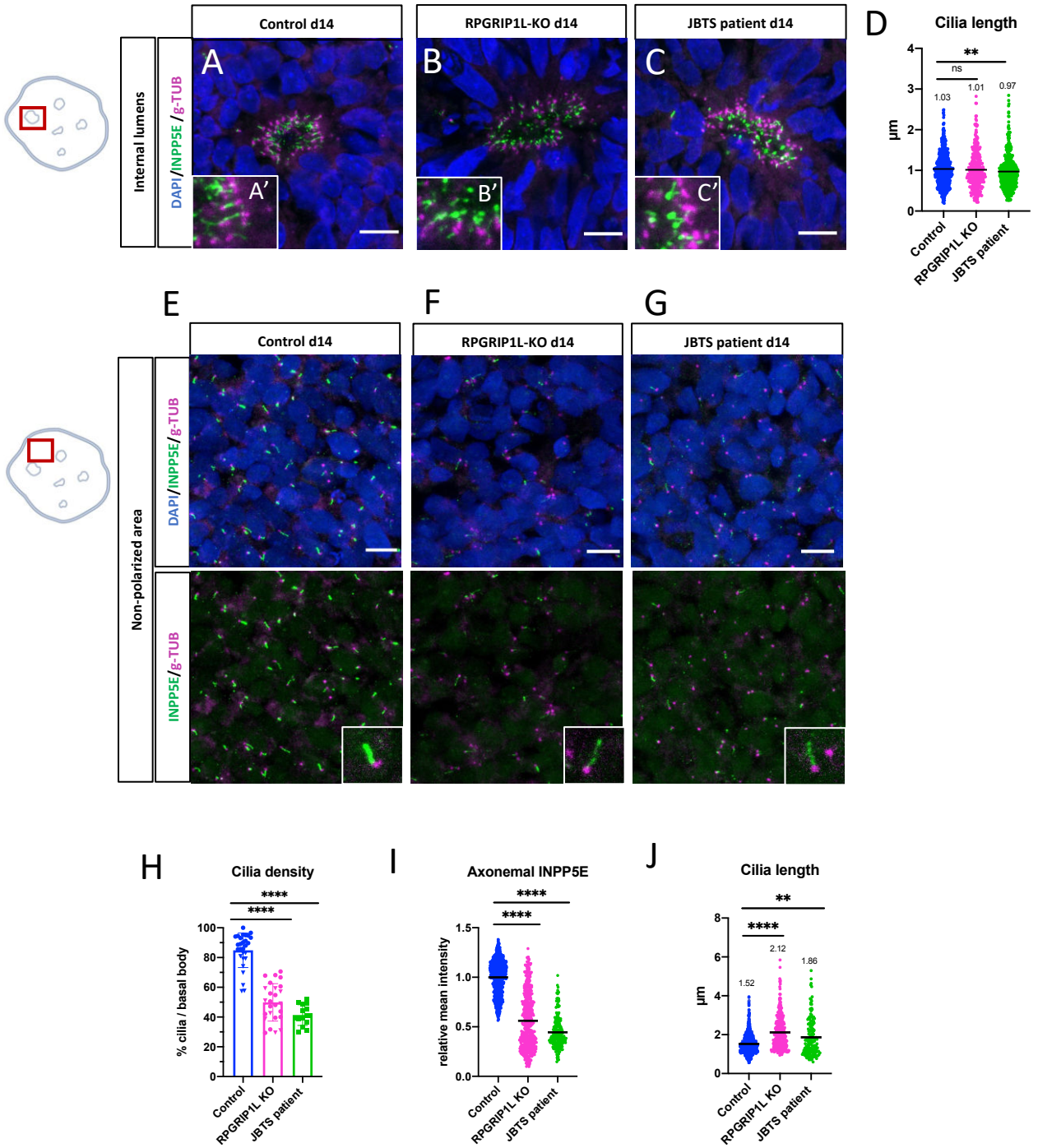
Control d14
RPGRIP1L-KO d14
JBTS patient d14
Internal lumens
DAPI/INPPSE /g-TUB
A
A'
B
B'
C
C'
D
Cilia length
µm
**
ns
1.03
1.01
0.97
Control
RPGRIP1L KO
JBTS patient
E
F
G
Non-polarized area
DAPI/INPP5E/g-TUB
INPP5E/g-TUB
H
Cilia density
% cilia / basal body
****
****
I
Axonemal INPP5E
relative mean intensity
****
****
J
Cilia length
µm
**
****
1.52
2.12
1.86

Figure 4

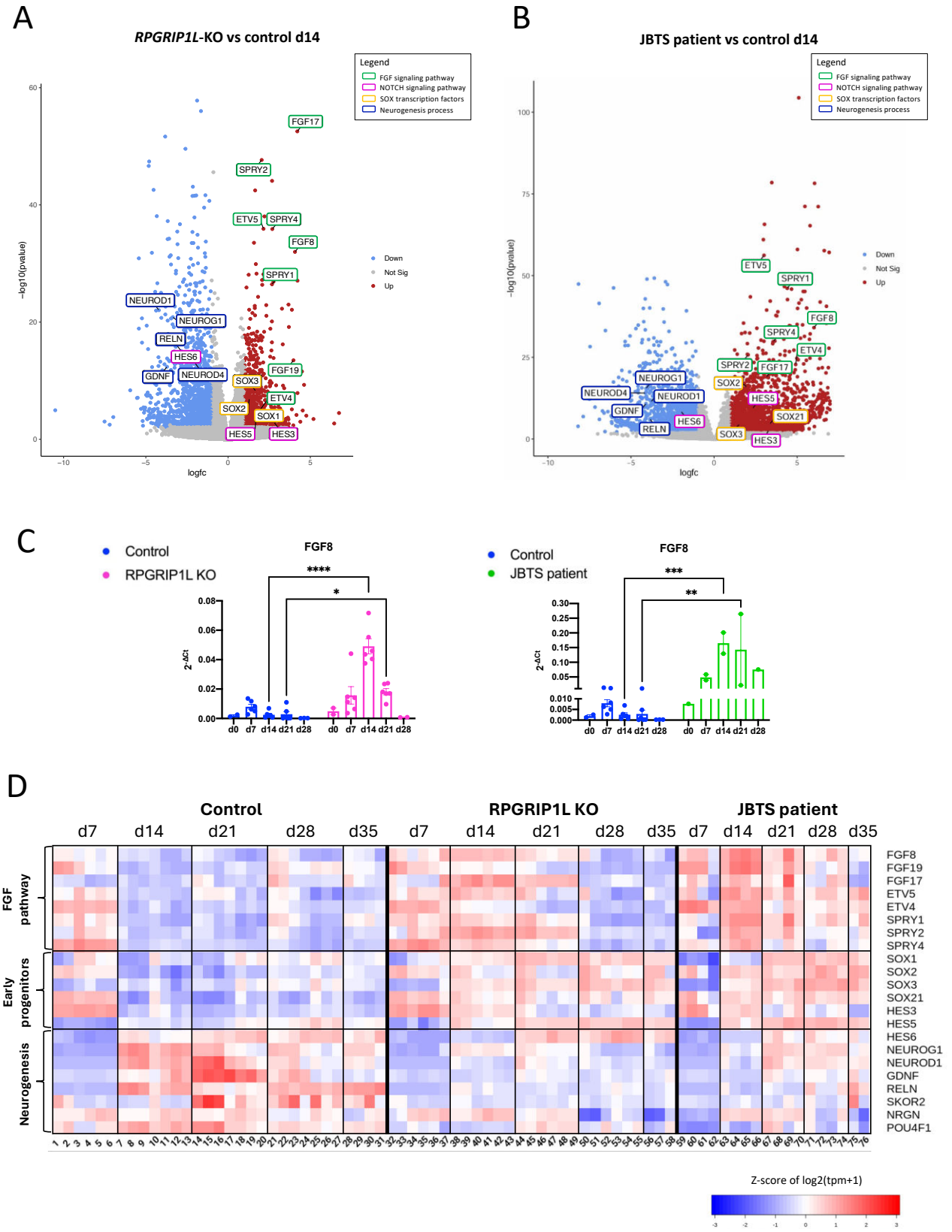
A
RPGRIP1L-KO vs control d14
Legend
FGF signaling pathway
NOTCH signaling pathway
SOX transcription factors
Neurogenesis process
Down
Not Sig
Up
FGF17
SPRY2
ETV5
SPRY4
FGF8
SPRY1
NEUROD1
NEUROG1
RELN
HES6
GDNF
NEUROD4
FGF19
SOX3
ETV4
SOX2
SOX1
HES5
HES3
−log10(pvalue)
logfc
B
JBTS patient vs control d14
ETV5
SPRY1
FGF8
SPRY4
ETV4
SPRY2
FGF17
SOX2
NEUROG1
NEUROD4
NEUROD1
HES5
GDNF
SOX21
HES6
RELN
SOX3
HES3
C
Control
RPGRIP1L KO
FGF8
****
*
2^-ΔCt
d0 d7 d14 d21 d28
Control
JBTS patient
FGF8
***
**
D
Control
RPGRIP1L KO
JBTS patient
d7 d14 d21 d28 d35
FGF pathway
Early progenitors
Neurogenesis
FGF8
FGF19
FGF17
ETV5
ETV4
SPRY1
SPRY2
SPRY4
SOX1
SOX2
SOX3
SOX21
HES3
HES5
HES6
NEUROG1
NEUROD1
GDNF
RELN
SKOR2
NRGN
POU4F1
Z-score of log2(tpm+1)

Figure 5

A

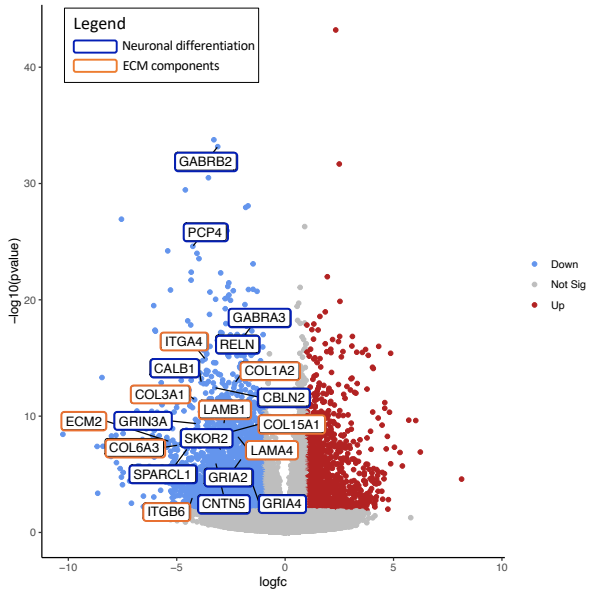

B

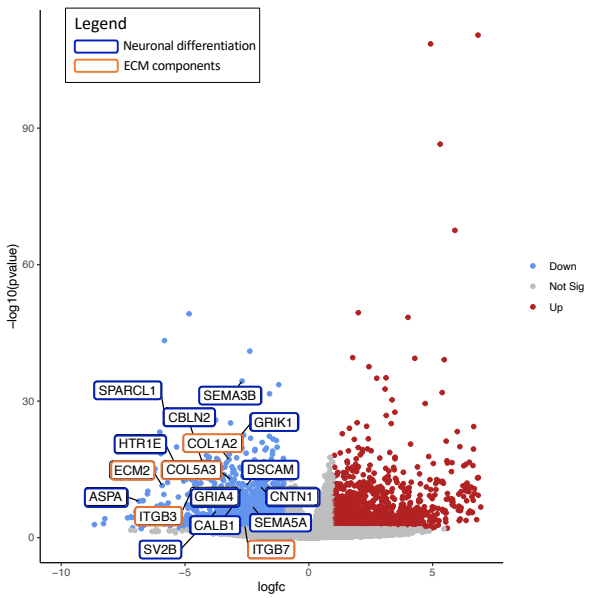

C

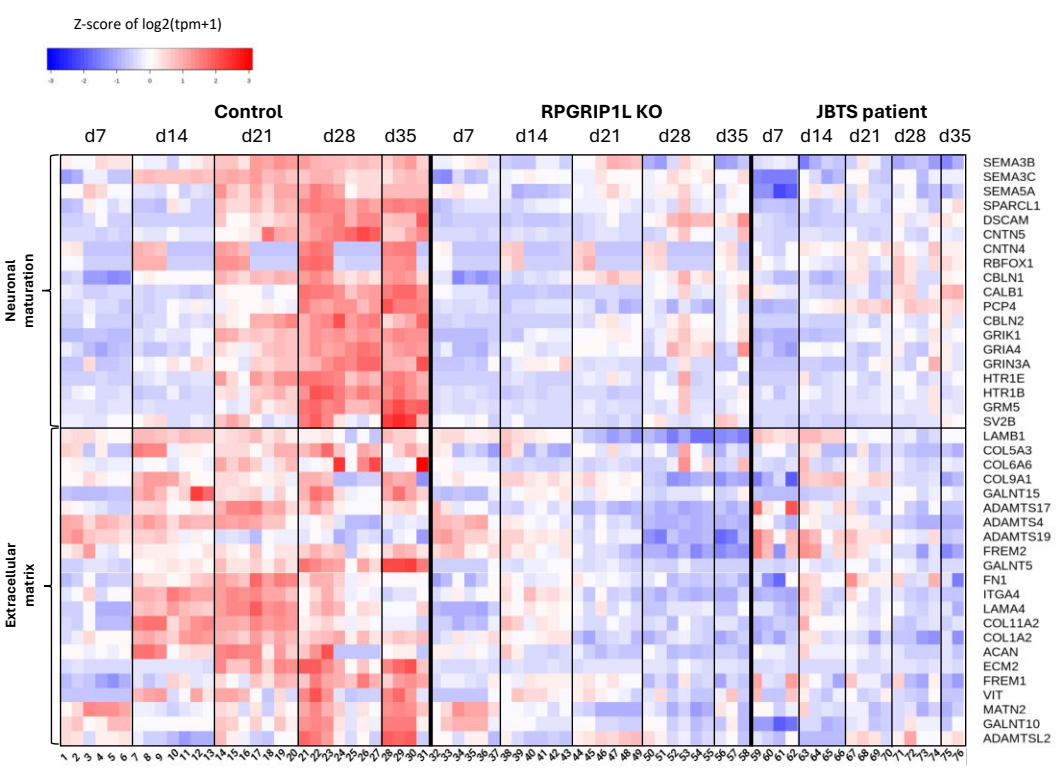

D

Day 28 in *RPGRIP1L KO* (negativeley enriched)

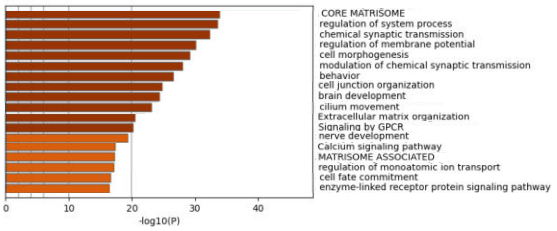

E

Day 28 in JBTS patient (negativeley enriched)

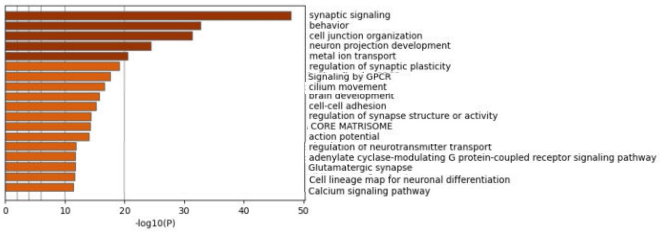

Figure 6

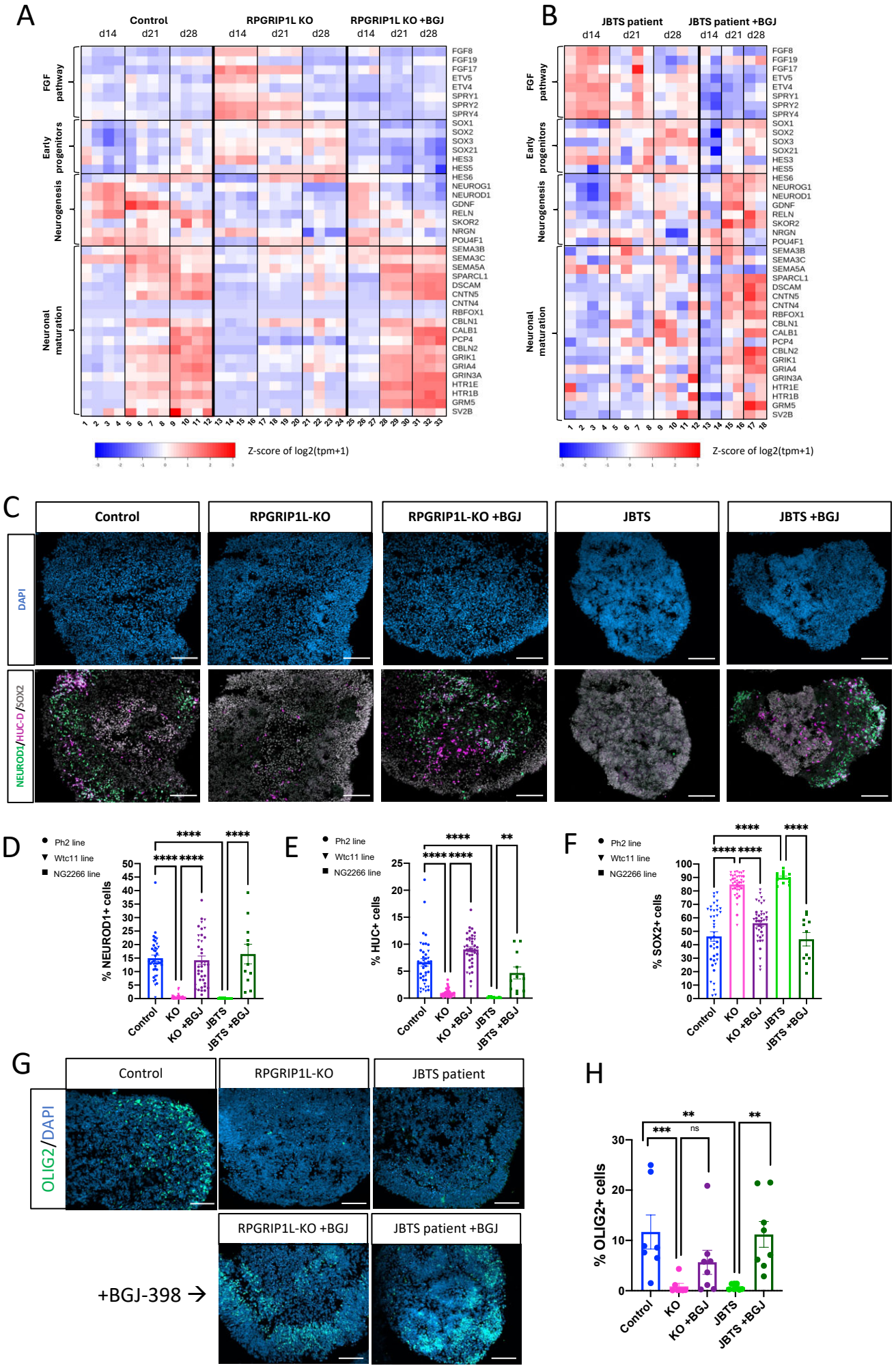
A
Control
RPGRIP1L KO
RPGRIP1L KO +BGJ
d14 d21 d28
FGF pathway
Early progenitors
Neurogenesis
Neuronal maturation
FGF8
FGF19
FGF17
ETV5
ETV4
SPRY1
SPRY2
SPRY4
SOX1
SOX2
SOX3
SOX21
HES3
HES5
HES6
NEUROG1
NEUROD1
GDNF
RELN
SKOR2
NRGN
POU4F1
SEMA3B
SEMA3C
SEMA5A
SPARCL1
DSCAM
CNTN5
CNTN4
RBFOX1
CBLN1
CALB1
PCP4
CBLN2
GRIK1
GRIA4
GRIN3A
HTR1E
HTR1B
GRM5
SV2B
Z-score of log2(tpm+1)
B
JBTS patient
JBTS patient +BGJ
d14 d21 d28
Z-score of log2(tpm+1)
C
Control
RPGRIP1L-KO
RPGRIP1L-KO +BGJ
JBTS
JBTS +BGJ
DAPI
NEUROD1/HUC-D/SOX2
D
Ph2 line
Wtc11 line
NG2266 line
% NEUROD1+ cells
Control
KO
KO +BGJ
JBTS
JBTS +BGJ
E
% HUC+ cells
F
% SOX2+ cells
G
Control
RPGRIP1L-KO
JBTS patient
OLIG2/DAPI
RPGRIP1L-KO +BGJ
JBTS patient +BGJ
+BGJ-398 →
H
% OLIG2+ cells
ns

Figure 7

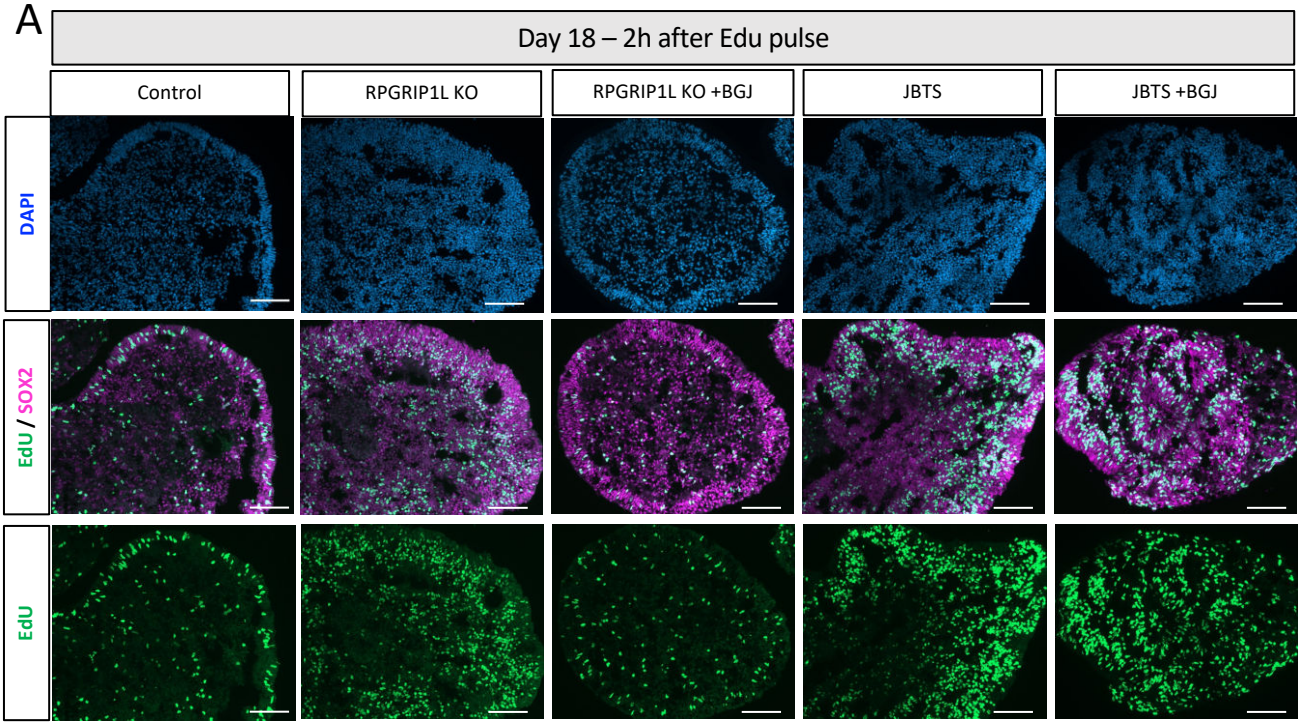
A
Day 18 – 2h after Edu pulse
Control
RPGRIP1L KO
RPGRIP1L KO +BGJ
JBTS
JBTS +BGJ
DAPI
EdU / SOX2
EdU

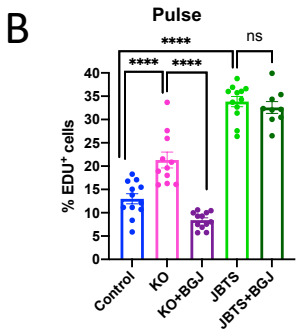
B
Pulse
% EDU+ cells
****
****
****
ns
Control
KO
KO+BGJ
JBTS
JBTS+BGJ

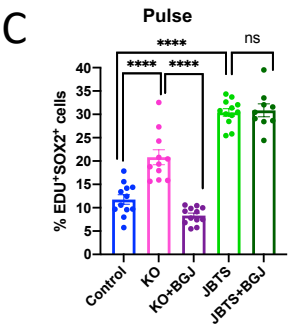
C
Pulse
% EDU+SOX2+ cells
****
****
****
ns
Control
KO
KO+BGJ
JBTS
JBTS+BGJ

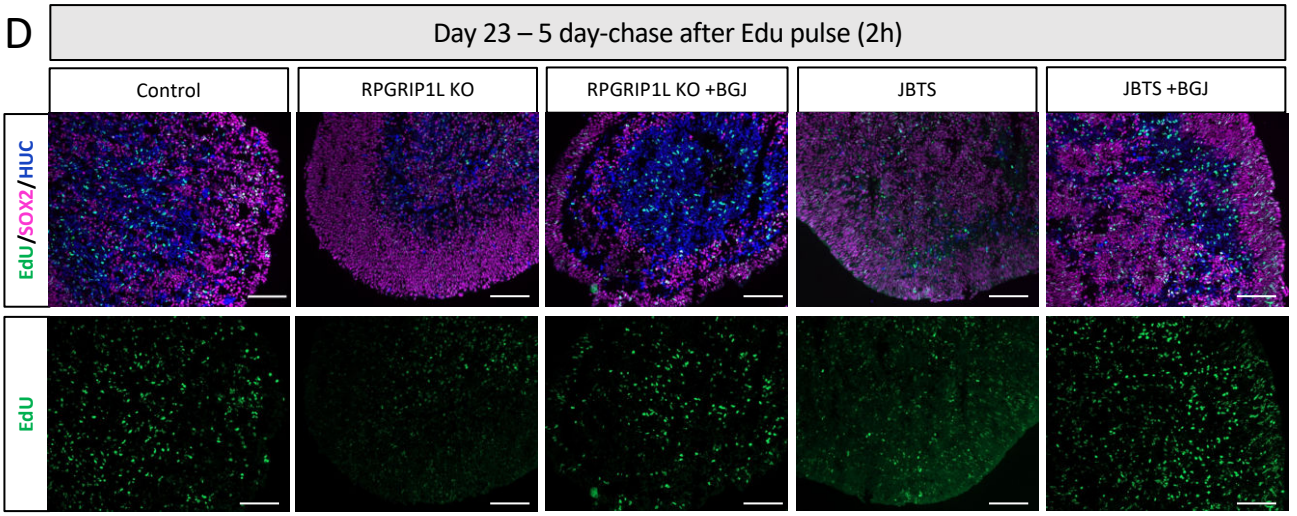
D
Day 23 – 5 day-chase after Edu pulse (2h)
Control
RPGRIP1L KO
RPGRIP1L KO +BGJ
JBTS
JBTS +BGJ
EdU/SOX2/HUC
EdU

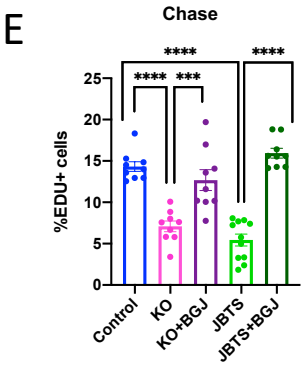
E
Chase
%EDU+ cells
****
****
***
****
Control
KO
KO+BGJ
JBTS
JBTS+BGJ

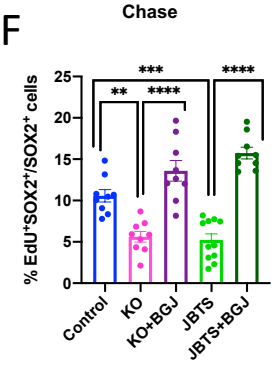
F
Chase
% EdU+SOX2+/SOX2+ cells
***
**
****
****
Control
KO
KO+BGJ
JBTS
JBTS+BGJ

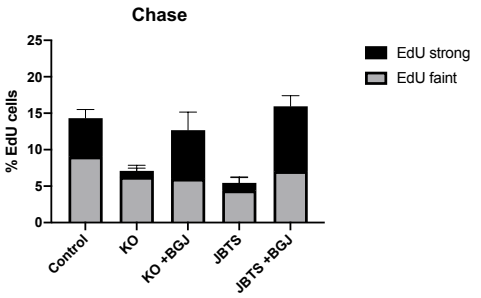
G
Chase
% EdU cells
EdU strong
EdU faint
Control
KO
KO +BGJ
JBTS
JBTS +BGJ

Supplementary Figure 1. Cerebellar organoids generated from control human induced pluripotent stem cells recapitulate early steps of cerebellar development

(A-C) Immunofluorescence for SOX2 (magenta, neural progenitors) and HUC/D (green, early-born neurons) on cryosections from control organoids at indicated time-points. **(D-G)** Graph showing normalized temporal gene expression analysis from bulk RNAseq data **(D)**: Purkinje cell markers: OLIG2, SKOR2, CALB1, **(E)** Glutamatergic lineage markers BARHL1, PAX6, ATOH1, **(F)** Granule Neuron marker (*GABRA6)*, and **(G)** *SHH*. Data are displayed as mean ± SEM and were obtained from both Ph2 and Wtc11 cell lines. Day 0 (hiPSCs): N=2; day 7-35 organoids: see Supplementary Table 2 for number of independent experimental replicates. **(H)** Immunofluorescence for BARHL1 (glutamatergic lineage marker) and CALB1 (Purkinje cell marker) on day 28 control organoid cryosection. Scale bars: 100 µm in A-C and H

Supplementary Figure 2. Altered RNA expression of Purkinje cell and glutamatergic lineage markers in *RPGRIP1L*-deficient cerebellar organoids

(A-C') Immunofluorescence for RPGRIP1L (in green), the ciliary marker ARL13B (in magenta) and the nuclear marker DAPI (blue, A, B, C) or the basal body marker GTUB (blue, A', B, C') on cryosections from control (A, A'), *RPGRIP1L* KO (B, B') and JBTS patient (C, C') organoids at day 21. Scale bars: 10 µm in A-C and 2 µm in A'-C'. **(D)** Graph showing normalized temporal gene expression analysis from bulk RNAseq data, displayed as mean ± SEM, of the Purkinje lineage markers *SKOR2, FOXP2, PDE1C* and *ITPR1* along the differentiation protocol. For control and *RPGRIP1L* KO conditions data were obtained from both Ph2 and Wtc11 cell lines. See Supplementary Table 2 for number of independent experimental replicates. **(E-F)** qPCR analysis of (E) the PC markers *OLIG2, SKOR2* and *CALB1* and (F) the glutamatergic lineage markers *PAX6, BARHL1, ATOH1*, in cerebellar organoids at different timepoints from several independent experiments. Each dot in the graph represents one independent experiment per timepoint and condition; circular dots represent Ph2 line, triangular dots represent Wtc11 line, squared dots represent NG2266 line. Mean ± SEM are shown. Asterisks denote statistical significance according to ordinary Two-Way ANOVA (*P<0.033, **P < 0.0021, ***P<0.0002 and ****P< 0.0001). **(G)** Immunofluorescence for ATOH1 (glutamatergic lineage) on cryosections from control, *RPGRIP1L* KO and JBTS patient organoid cryosections at day 28. **(H)** Graph showing the % of ATOH1-positive cells over the total number of nuclei stained with DAPI. Positive cells were counted in more than 15 sections from different organoids per

experiment per condition. Control and *RPGRIP1L* KO: N=3 (Ph2 N=2, Wtc11 N=1); JBTS patient: NG2266 N=2). Data are shown as individual values. Mean ± SEM are indicated. Asterisks denote statistical significance according to One-Way ANOVA Kruskal-Wallis test with Dunn's correction (****P<0.0001). **(I-K)** Graphs showing the average intensity of CALB1 (I), BARHL1 (J), ATOH1 (K) labeling on cryosections from control, *RPGRIP1L* KO and JBTS organoids at day 28. Average cell intensity was measured in more than 15 sections from different organoids per experiment per condition. Relative mean intensity was calculated considering the mean intensity in control organoid sections as the reference value (1). Data are shown as individual values. Mean ± SEM are indicated; circular dots represent Ph2 line, triangular dots represent Wtc11 line, squared dots represent NG2266 line. Asterisks denote statistical significance according to One-Way ANOVA Kruskal-Wallis test with Dunn's correction (*P<0.033, and ****P<0.0001). N: number of independent experimental replicates. Scale bars: 100 µm in H.

Supplementary Figure 3. FGF8 protein localization at the apical sides of early neural progenitors

(A-C) Immunofluorescence for SOX2 (in magenta) and FGF8 (in green) on cryosections from day 14 control (A), *RPGRIP1L* KO (B) and JBTS patient (C) organoids. Scale bar, 100 µm. **(D-H)** Confocal images of FGF8 (green) and ZO1 (red) immunofluorescence showing accumulation of FGF8 protein at ZO1+ apical sides of progenitor rosettes in control (D), *RPGRIP1L* KO (E) and JBTS patient (F) organoids. *RPGRIP1L* KO (G) and JBTS patient (H) organoids also present FGF8 protein accumulation at ZO1+ apical junctions at the organoid borders. Scale bars: 100 µm in A and 10 µm in B-F.

Supplementary Figure 4. FGF signaling inhibition rescues organoid size and gene expression in *RPGRIP1L* deficient organoids.

(A) Scheme representing the experimental plan for organoid treatment with FGFR-inhibitor (BGJ-398) along the 3D cerebellar differentiation protocol. Arrows on the top represent the timepoints of BGJ-398 pulses. Arrows at the bottom indicate the timepoints at which organoids were collected after receiving BGJ-398 treatment. **(B)** Graph representing the growth rate of cerebellar organoids (left) and representative bright field images of cerebellar organoids at day 28 (right). Organoid area was measured every 7 days from day 7 to day 35 of the differentiation protocol. Data are shown as the mean ± SEM of average organoid area

from several independent experiments. Control and *RPGRIP1L* KO: N=3 (Wtc11), JBTS patient: N=1 (NG2266 line); n=10-60 organoids analyzed per experiment per condition. Scale bar, 500 µm. **(C)** Heatmap representation of the normalized gene expression values of selected differentially expressed genes in control and *RPGRIP1L*-deficient, untreated or treated with BGJ-398, cerebellar organoids over time. Sample numbering at the bottom is explained in Supplementary Table 3. Control: N=4 for days 14, 21 and 28; *RPGRIP1L* KO untreated: N=4 for days 14, 21 and 28; RPGRIP1L KO BGJ-treated : N=3 for days 14, 21 and 28. At least 20 organoids were analyzed per experiment per condition. **(D)** Heatmap representation of the normalized gene expression values over time of selected differentially expressed genes in JBTS patient-derived cerebellar organoids, untreated or treated with BGJ-398, as indicated on top. Sample numbering at the bottom is explained in Supplementary Table 4. JBTS patient organoids untreated: N=4 for days 14, 21 and 28; JBTS patient organoids BGJ-treated : N=2 for days 14, 21 and 28. At least 20 organoids were analyzed per experiment per condition. **(E-L)** Graphs showing gene expression levels by qPCR analysis of *FGF8* (E), *ETV4* (F) *ETV5* (G), *SPRY1* (H), *NEUROD1* (I), *NEUROG1* (J), *SKOR2* (K) and *CALB1* (L) in control and *RPGRIP1L*-deficient, untreated or treated with BGJ-398, cerebellar organoids at different timepoints. Data are shown as individual values from independent experiments, mean ± SEM are indicated. For (E-G, L) control and *RPGRIP1L* KO: N=4 (Wtc11); JBTS patient: N=2 (NG2266). For (H-K) control and *RPGRIP1L* KO: N=3 (Wtc11); JBTS patient: N=1 (NG2266). N: number of independent experimental replicates.

Supplementary Figure 5. NG2266 splice variant c.2304+1G>T results in intron retention.

(A) Schematic representation of *RPGRIP1L* gene exons 14-18 and PCR primers position to analyze cDNA products of *RPGRIP1L* gene in JBTS patient cells (NG2266 line) compared to control (Ph2 line). **(B)** PCR products from JBTS patient and control cerebellar cDNAs, templated by primer pairs as indicated, were analyzed by agarose gel electrophoresis and visualized with ethidium bromide. The primer pair 1-2 only amplifies JBTS patient cDNA, showing intron 16-17 retention. The primer pair 1-3 amplify both the second JBTS patient allele (encoding the *RPGRIP1L* Q684X variant) and control cDNA. **(C)** Sequence of the PCR product templated by primer pair 1-2 on cDNA derived from NG2266 cell line.

Supplementary Figure 1

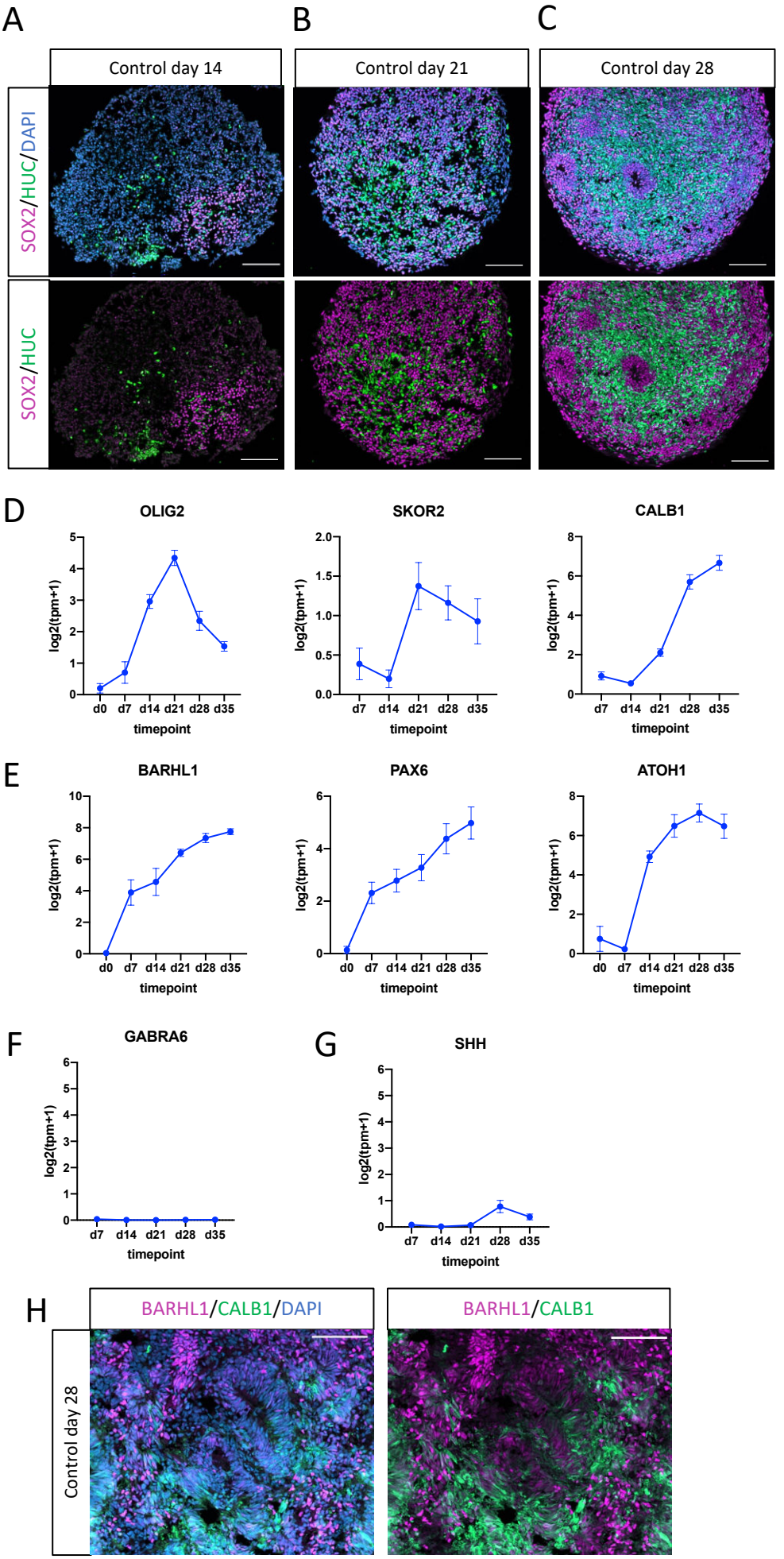

Supplementary Figure 2

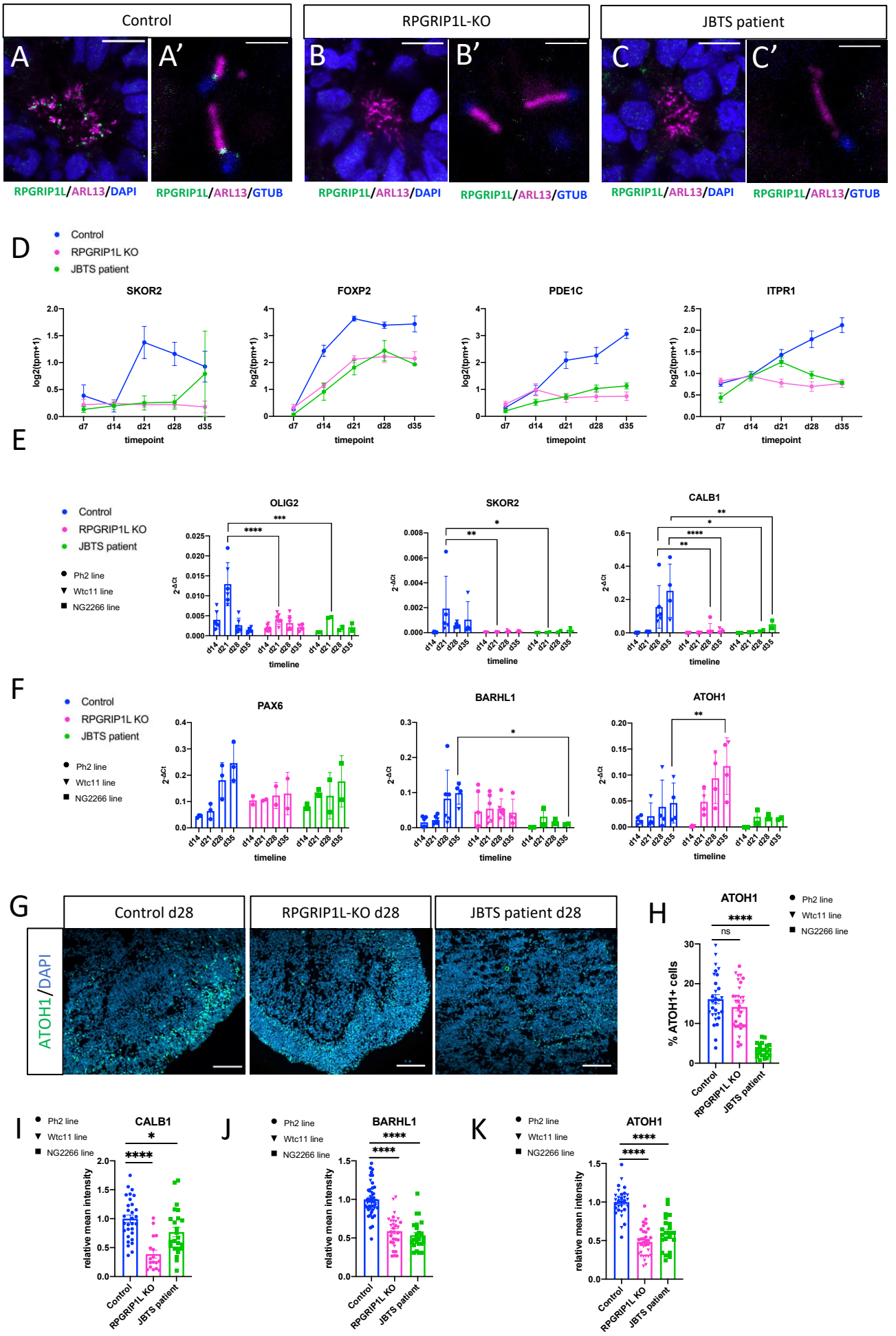

Supplementary Figure 3

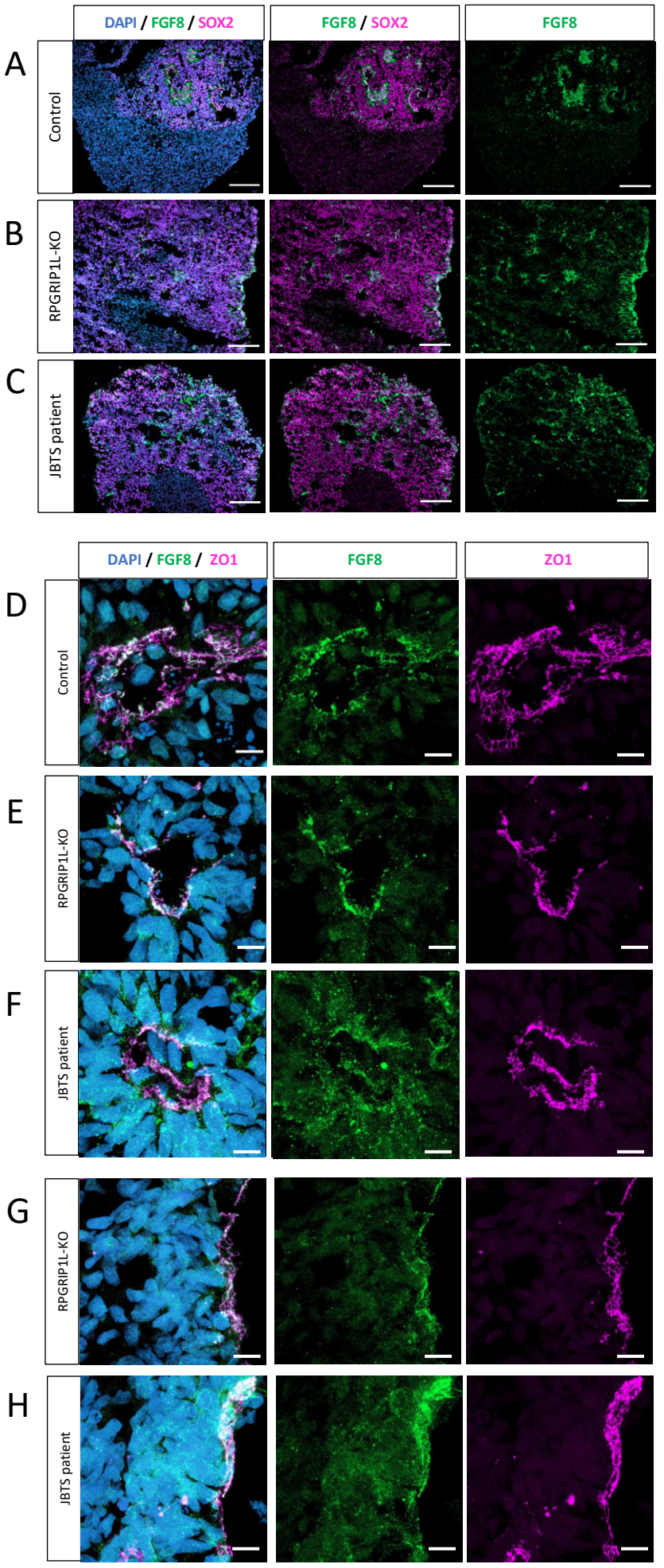

Supplementary Figure 4

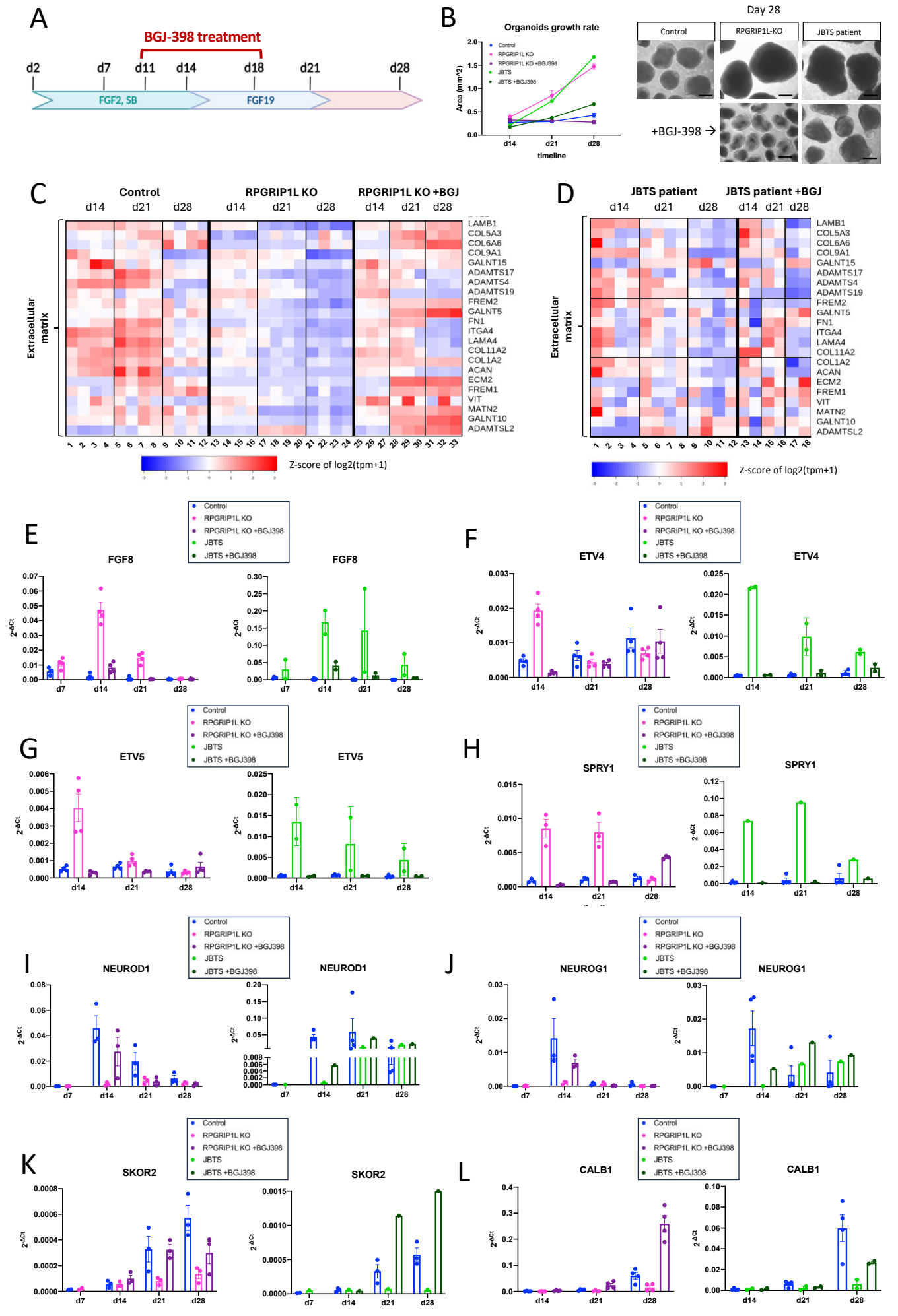

Supplementary Figure 5

A

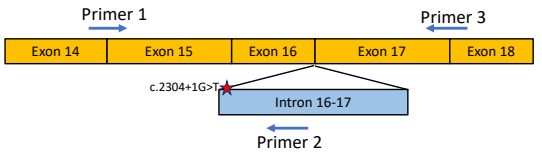

B

B’

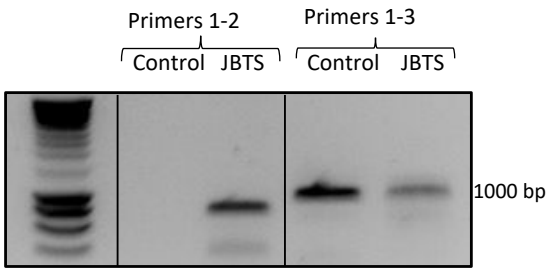

C

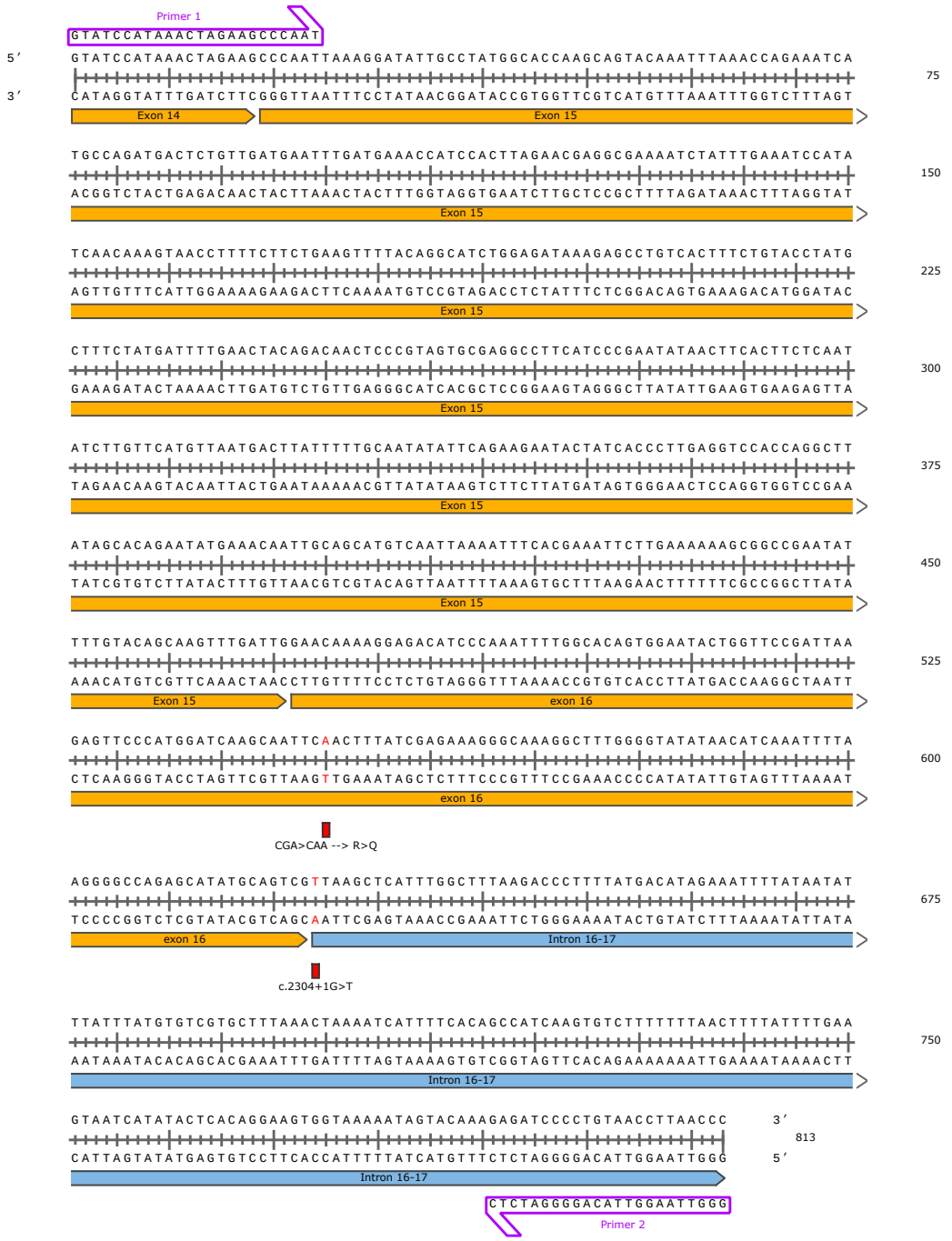

Supplementary Table 1.

Label	Condition	N per timepont	Cell line	Sample name
1	Control	Day 7 N=6	Ph2 cell line	CBI-ph2-25-WT-d7
2				CBII-ph2-25-WT-d7
3			wtc11 cell line	CBIV-wtc11-19-WT-d7
4				CBV-wtc11-19-WT-d7
5				CBVI-wtc11-19-WT-d7
6				CBVII-wtc11-19-WT-d7
7	RPGRIP1L KO	Day 7 N=6	Ph2 cell line	CBI-ph2-44-KO-d7
8				CBII-ph2-44-KO-d7
9			wtc11 cell line	CBIV-wtc11-65-KO-d7
10				CBV-wtc11-65-KO-d7
11				CBVI-wtc11-65-KO-d7
12				CBVII-wtc11-65-KO-d7
13	JBTS patient	Day 7 N=4	NG2266 JBTS patient derived cell line	CBI-NG-2266-d7
14				CBII-NG-2266-d7
15				CBVII-NG-2266-d7
16				CBVIII-NG-2266-d7

Supplementary Table 2.

Label	Condition	N per timepont	Cell line	Sample name
1	Control	Day 7 N=6	Ph2 cell line	CBI-ph2-25-WT-d7
2				CBII-ph2-25-WT-d7
3			wtc11 cell line	CBIV-wtc11-19-WT-d7
4				CBV-wtc11-19-WT-d7
5				CBVI-wtc11-19-WT-d7
6				CBVII-wtc11-19-WT-d7
7		Day 14 N=7	Ph2 cell line	CBI-ph2-25-WT-d14
8				CBII-ph2-25-WT-d14
9				CBIII-ph2-25-WT-d14
10			wtc11 cell line	CBIV-wtc11-19-WT-d14
11				CBV-wtc11-19-WT-d14
12				CBVI-wtc11-19-WT-d14
13				CBVII-wtc11-19-WT-d14
14		Day 21 N=7	Ph2 cell line	CBI-ph2-25-WT-d21
15				CBII-ph2-25-WT-d21
16				CBIII-ph2-25-WT-d21
17			wtc11 cell line	CBIV-wtc11-19-WT-d21
18				CBV-wtc11-19-WT-d21
19				CBVI-wtc11-19-WT-d21
20				CBVII-wtc11-19-WT-d21
21		Day 28 N=7	Ph2 cell line	CBI-ph2-25-WT-d28

22				CBII-ph2-25-WT-d28
23				CBIII-ph2-25-WT-d28
24			wtc11 cell line	CBIV-wtc11-19-WT-d28
25				CBV-wtc11-19-WT-d28
26				CBVI-wtc11-19-WT-d28
27				CBVII-wtc11-19-WT-d28
28		Day 35 N=4	Ph2 cell line	CBI-ph2-25-WT-d35
29				CBII-ph2-25-WT-d35
30				CBIII-ph2-25-WT-d35
31			wtc11	CBIV-wtc11-19-WT-d35
32	RPGRIP1L KO	Day 7 N=6	Ph2 cell line	CBI-ph2-44-KO-d7
33				CBII-ph2-44-KO-d7
34			wtc11 cell line	CBIV-wtc11-65-KO-d7
35				CBV-wtc11-65-KO-d7
36				CBVI-wtc11-65-KO-d7
37				CBVII-wtc11-65-KO-d7
38		Day 14 N=6	Ph2 cell line	CBI-ph2-44-KO-d14
39				CBII-ph2-44-KO-d14
40			wtc11 cell line	CBIV-wtc11-65-KO-d14
41				CBV-wtc11-65-KO-d14
42				CBVI-wtc11-65-KO-d14
43				CBVII-wtc11-65-KO-d14
44		Day 21 N=6	Ph2 cell line	CBI-ph2-44-KO-d21
45				CBII-ph2-44-KO-d21
46			wtc11 cell line	CBIV-wtc11-65-KO-d21
47				CBV-wtc11-65-KO-d21
48				CBVI-wtc11-65-KO-d21
49				CBVII-wtc11-65-KO-d21
50		Day 28 N=6	Ph2 cell line	CBI-ph2-44-KO-d28
51				CBII-ph2-44-KO-d28
52			wtc11 cell line	CBIV-wtc11-65-KO-d28
53				CBV-wtc11-65-KO-d28
54				CBVI-wtc11-65-KO-d28
55				CBVII-wtc11-65-KO-d28
56		Day 35 N=3	Ph2 cell line	CBI-ph2-44-KO-d35
57				CBII-ph2-44-KO-d35
58			wtc11	CBIV-wtc11-65-KO-d35
59	JBTS patient	Day 7 N=4	NG2266 JBTS patient derived cell line	CBI-NG-2266-d7
60				CBII-NG-2266-d7
61				CBVII-NG-2266-d7
62				CBVIII-NG-2266-d7
63		Day 14 N=4		CBI-NG-2266-d14
64				CBII-NG-2266-d14
65				CBVII-NG-2266-d14
66				CBVIII-NG-2266-d14

67		Day 21 N=4		CBI-NG-2266-d21
68				CBII-NG-2266-d21
69				CBVII-NG-2266-d21
70				CBVIII-NG-2266-d21
71		Day 28 N=4		CBI-NG-2266-d28
72				CBII-NG-2266-d28
73				CBVII-NG-2266-d28
74				CBVIII-NG-2266-d28
75		Day 35 N=2		CBI-NG-2266-d35
76				CBII-NG-2266-d35

Supplementary Table 3.

Label	Cell line	Condition	N per timepont	Sample name
1	wtc11 cell line	Control	Day 14 N=4	CBIV-wtc11-19-WT-d14
2				CBV-wtc11-19-WT-d14
3				CBVI-wtc11-19-WT-d14
4				CBVII-wtc11-19-WT-d14
5			Day 21 N=4	CBIV-wtc11-19-WT-d21
6				CBV-wtc11-19-WT-d21
7				CBVI-wtc11-19-WT-d21
8				CBVII-wtc11-19-WT-d21
9			Day 28 N=4	CBIV-wtc11-19-WT-d28
10				CBV-wtc11-19-WT-d28
11				CBVI-wtc11-19-WT-d28
12				CBVII-wtc11-19-WT-d28
13		RPGRIP1L KO	Day 14 N=4	CBIV-wtc11-65-KO-d14
14				CBV-wtc11-65-KO-d14
15				CBVI-wtc11-65-KO-d14
16				CBVII-wtc11-65-KO-d14
17			Day 21 N=4	CBIV-wtc11-65-KO-d21
18				CBV-wtc11-65-KO-d21
19				CBVI-wtc11-65-KO-d21
20				CBVII-wtc11-65-KO-d21
21			Day 28 N=4	CBIV-wtc11-65-KO-d28
22				CBV-wtc11-65-KO-d28
23				CBVI-wtc11-65-KO-d28
24				CBVII-wtc11-65-KO-d28
25		RPGRIP1L KO +BGJ398 treatment	Day 14 N=3	CBV-wtc11-65-KO-BGJ-d14
26				CBVI-wtc11-65-KO-BGJ-d14
27				CBVII-wtc11-65-KO-BGJ-d14
28			Day 21 N=3	CBV-wtc11-65-KO-BGJ-d21
29				CBVI-wtc11-65-KO-BGJ-d21
30				CBVII-wtc11-65-KO-BGJ-d21

31			Day 28 N=3	CBV-wtc11-65-KO-BGJ-d28
32				CBVI-wtc11-65-KO-BGJ-d28
33				CBVII-wtc11-65-KO-BGJ-d28

Supplementary Table 4.

Label	Cell line	Condition	N per timepont	Sample name
1	NG2266 JBTS patient derived cell line	NG2266 untreated	Day 14 N=4	CBI-NG-2266-d14
2				CBII-NG-2266-d14
3				CBVII-NG-2266-d14
4				CBVIII-NG-2266-d14
5			Day 21 N=4	CBI-NG-2266-d21
6				CBII-NG-2266-d21
7				CBVII-NG-2266-d21
8				CBVIII-NG-2266-d21
9			Day 28 N=4	CBI-NG-2266-d28
10				CBII-NG-2266-d28
11				CBVII-NG-2266-d28
12				CBVIII-NG-2266-d28
13		NG2266 +BGJ398 treatment	Day 14 N=2	CBVII-NG-2266-BGJ-d14
14				CBVIII-NG-2266-BGJ-d14
15			Day 21 N=2	CBVII-NG-2266-BGJ-d21
16				CBVIII-NG-2266-BGJ-d21
17			Day 28 N=2	CBVII-NG-2266-BGJ-d28
18				CBVIII-NG-2266-BGJ-d28

Supplementary Table 5.

primary Antibody	host	company	reference	dilution
Atoh1(Math1)	rabbit	Cohesion Biosciences	CQA1401	1:200
Barhl1	rabbit	Atlas	HPA004809	1:300
Calbindin	rabbit	Swant	CB-38	1:300
Fgf8	mouse IgG1	ReD system	MAB323	1:40
HuC/HuD (16A11) Elav	mouse IgG2b	Molecular Probes	A-21271	1:200
Inpp5e	rabbit	Proteintech	17797-1-AP	1:300
NeuroD1	mouse IgG1	Proteintech	66691-1-Ig	1:200
Olig2	rabbit	Millipore	AB9610	1:200
Sox2	rabbit	Millipore	AB5603	1:200
Zo1	rabbit	Life technologie	617300	1:300
γ-Tubulin	mouse IgG1	Sigma	T6557	1:500

Supplementary Table 6.

secondary Antibody	host	conjugate	company
Mouse IgG1	goat	Alexa488	Molecular Probes
Mouse IgG1	goat	Alexa633	Molecular Probes
Mouse IgG2b	goat	Alexa568	Molecular Probes
Rabbit	goat	Alexa488	Molecular Probes
Rabbit	goat	Alexa568	Molecular Probes
Rabbit	goat	Alexa633	Molecular Probes

Supplementary Table 7.

Gene	Forward	Reverse
ATOH1	GTTATCCCGTCGTTCAACAACG	TGGGCGTTTGTAGCAGCTC
BARHL1	CGCGGAGGACTTTAGAGACAA	AGCTGGAGATCTCGCGGTC
CALB1	GGAAGTGGTTACCTGGAAGGA	CTCTTTGCCCATACTGATCCAC
ETV4	GTGGTGATCAAACAGGAACAGAC	TGTGTGGAGGTACATTGATGCG
ETV5	TGTTGTGCCTGAGAGACTGGA	GGTCATCAAGAAGGGTGACCA
FGF8	GACCCCTTCGCAAAGCTCAT	CCGTTGCTCTTGGCGATCA
GAPDH	CAACGGATTTGGTCGTATTGG	GCAACAATATCCACTTTACCAGAGTTA
NEUROD1	ATCATGAGCGAGTCATGAGTGC	GCACAGTGGGTTCGTTTCCC
NEUROG1	CCCTAGTCAGCAGGCAATAGAT	TCAGGTATCCCCGACTGCTTTA
OLIG2	GGGCCACAAGTTAGTTGGAA	GAGGAACGGCCACAGTTCTA
PAX6	TGCGACATTTCCCGAATTCTGC	CAGTCTCGTAATACCTGCCCA
SKOR2	ACACGCCTAAAGACACCCAG	ACGCCAGCAGGATGTCGTT
SPRY1	CTTTGCATTAGGCATTTCGGCC	ATTCCGCACGTTGGGCAAGT
SPRY4	CTCCTCAAAGGCCCCTAGAA	GGCTGGACCATGACTGAGTT